Check for updates

MATERIALS SCIENCE

A biofilm-derived peptide as an underwater adhesive

Xin Huang[1,2], Ewelina D. Liszczyk[1,3], Ramesh Prasad[4], Megan E. Mitchell[5,6], Zhijie Wang[2], Yuchu Liu[1], Sarvagya Saluja[1], Mingyu Wang[3], Rebekah A. Jackson[2], Peter Dahl[7,8], Roberto Andresen Eguiluz[9], Nikhil Malvankar[7,8], Elsa C. Y. Yan[2], Rich Olson[3], Huan-Xiang Zhou[4,10], Jing Yan[1,11]*

Copyright © 2026 The Authors, some rights reserved; exclusive licensee American Association for the Advancement of Science. No claim to original U.S. Government Works. Distributed under a Creative Commons Attribution NonCommercial License 4.0 (CC BY-NC).

Wet adhesives that perform under water have broad applications in industrial and biomedical settings. To date, molecular designs for underwater adhesives have largely been inspired by marine animals including mussels and barnacles. Here, we propose bacterial biofilms as an alternative source of inspiration for underwater adhesives. Specifically, we demonstrate the application potential of a peptide derived from biofilms formed by the notorious pathogen *Vibrio cholerae*. We characterize the ability of this biofilm-derived peptide to adsorb onto various surfaces and to glue wet surfaces by using a combination of confocal microscopy, molecular dynamics simulations, atomic force microscopy, lap shear tests, and spectroscopic tools. We further show that the peptide can coaggregate with microspheres acting as an effective flocculant. Our results open new design possibilities for underwater adhesives inspired by natural biofilms.

INTRODUCTION

Adhesives play important roles in daily life, industrial operations, and biomedical devices (*1*, *2*). They are generally composed of viscoelastic polymers and are most often applied to clean, dry surfaces. However, many important applications require glues that can be applied and function under wet conditions, such as the repair of submarine vehicles and instruments or the use of tissue adhesives for suture-less wound closure (*2*, *3*). Conventional glues based on synthetic polymers generally perform less well in a wet, complex environment; hence, there is a clear need for new adhesives that can be applied in these conditions. To identify better adhesive materials that function in aqueous environments, extensive studies have been focused on adhesive proteins from various marine animals, particularly mussels, yielding major insights into biological adhesion (*4*–*8*). The key molecular moiety underlying the adhesive function of mussel foot proteins (Mfps) is L-3,4-dihydroxyphenylalanine (L-DOPA), produced from the amino acid L-tyrosine by the enzyme tyrosinase. The catechol group of DOPA, consisting of a benzene ring with two hydroxyl groups, supports multiple modes of interaction with surfaces, including hydrogen bonding, metal coordination, π-π, amino-π, and cation-π interactions (*9*, *10*). Inspired by the design and adhesive performance of Mfps, purified variations of Mfps and synthetic polymers with integrated DOPA units have been used for underwater adhesive applications (*11*–*17*). However, because of the inherent chemical reactivity of DOPA, Mfps are sensitive to environmental conditions, including oxygen and pH, limiting both their performance in challenging complex environments and a fundamental understanding of the adhesive mechanism. Alternative bioinspired adhesion strategies have also been explored on the basis of barnacles (*18*), ticks (*19*), sea anemone (*20*), starfish (*21*), tunicates (*22*), octopus (*23*), among others.

In this work, we turned to an alternative, untapped source of bioinspiration for underwater adhesion: biofilms. Biofilms are surface-associated bacterial communities encased in an extracellular polymeric matrix (*24*–*27*). While many bacteria rely on this lifestyle for their survival, biofilms are also widely found in infections and biofouling (*28*, *29*). Bacteria have evolved for billions of years a surface-associated lifestyle and have consequently developed versatile underwater glues. In particular, *Vibrios* are a major genus among marine bacteria and have adapted to form biofilms on various marine surfaces in salty environments (*30*–*32*). In a prior study of biofilms formed by *Vibrio cholerae*, the causal agent of the pandemic cholera (*32*, *33*), we found that two partially redundant matrix proteins, Bap1 and RbmC, behave as double-sided tape to anchor *V. cholerae* biofilm clusters to host and environmental surfaces (*34*, *35*). The major matrix component in *V. cholerae* biofilms, *Vibrio* polysaccharide (VPS), does not confer adhesion to foreign surfaces by itself; instead, the two adhesins bind to VPS via a conserved β-propeller domain while containing a diverse set of surface-binding functionalities in their environment-facing domains. Specifically, Bap1 adheres to abiotic surfaces and lipid membranes via a 57–amino acid loop (hitherto called Bap1-57aa) nested in a β-prism domain. In contrast, RbmC has several domains targeting O-glycan–containing mucins and complex N-glycans prevalent in host cell-surface proteins (*36*). Together, Bap1 and RbmC play critical roles in enabling *V. cholerae* biofilms to attach to environmental and host cell surfaces (*34*, *35*, *37*), enhancing colonization and potentially pathogenicity of *V. cholerae* (*38*–*42*).

Bap1-57aa is largely responsible for the ability of *V. cholerae* biofilms to adhere to different abiotic substrata (Fig. 1A) (*34*). A chemically synthesized peptide with the Bap1-57aa sequence can spontaneously bind to lipid membranes and glass surfaces outside the biofilm context, suggesting that the Bap1-57aa peptide may serve as a generic and readily tunable underwater glue. In this manuscript, we characterize the ability of this biofilm-derived peptide and its variants to adsorb onto various surfaces and evaluate their potential as underwater adhesives by using

[1]Department of Molecular, Cellular and Developmental Biology, Yale University, New Haven, CT 06511, USA. [2] Department of Chemistry, Yale University, New Haven, CT 06520, USA. [3]Department of Molecular Biology and Biochemistry, Molecular Biophysics Program, Wesleyan University, Middletown, CT 06459, USA. [4]Department of Chemistry, University of Illinois Chicago, Chicago, IL 60607, USA. [5]National Institute of Standards and Technology, Gaithersburg, MD 20899, USA. [6]A. James Clark School of Engineering, University of Maryland, College Park, MD 20742, USA. [7]Department of Molecular Biophysics and Biochemistry, Yale University, New Haven, CT 06511, USA. [8]Microbial Sciences Institute, Yale University, West Haven, CT 06516, USA. [9]Department of Chemical and Materials Engineering, University of California Merced, Merced, CA 95344, USA. [10]Department of Physics, University of Illinois Chicago, Chicago, IL 60607, USA. [11]Quantitative Biology Institute, Yale University, New Haven, CT 06511, USA.
*Corresponding author. Email: jing.yan@yale.edu

Downloaded from https://www.science.org on November 20, 2026

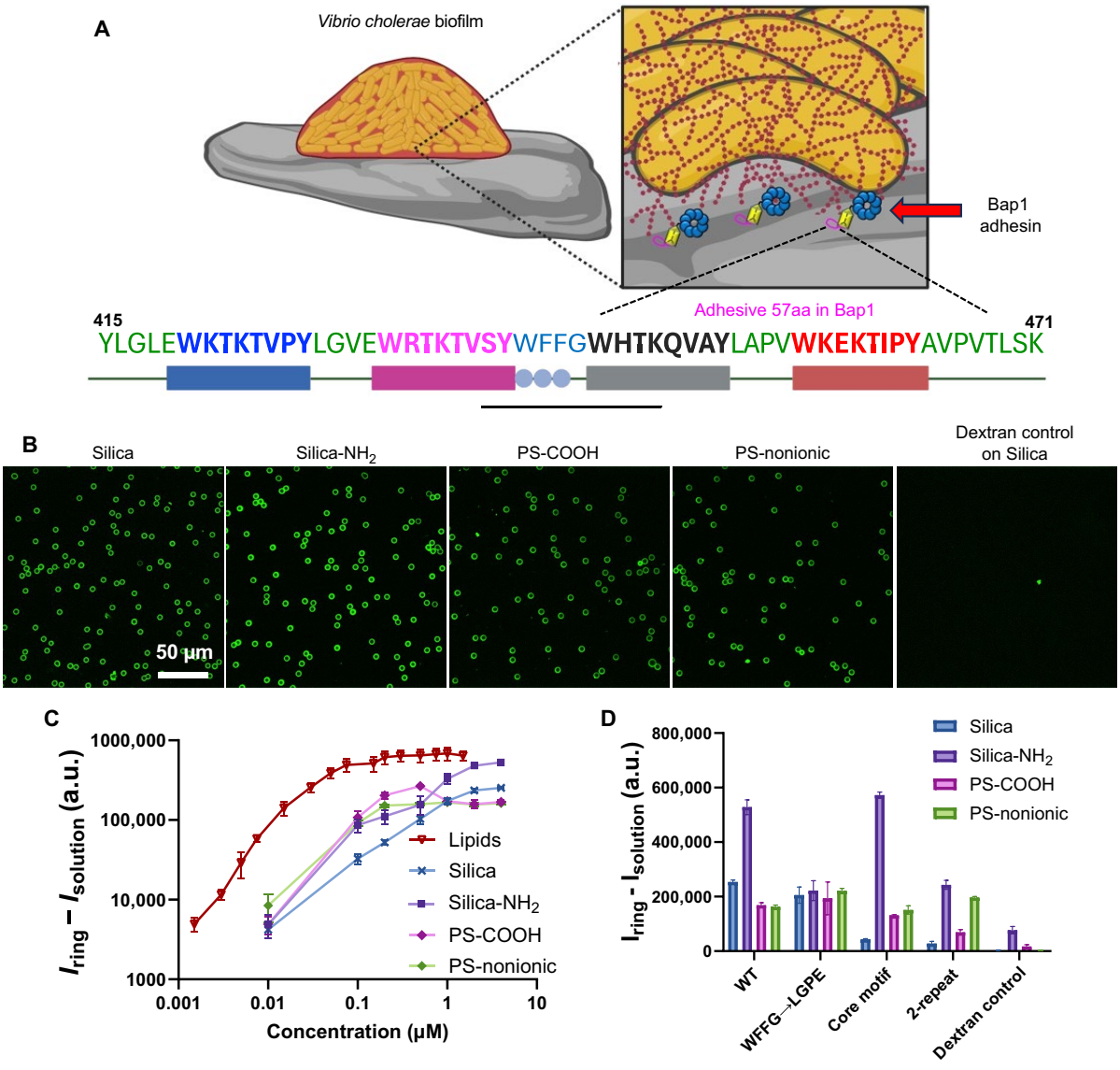


Fig. 1. The biofilm-derived Bap1-57aa peptide adsorbs to a wide range of surfaces. (**A**) Schematic of *V. cholerae* biofilms adhering to an abiotic surface. Yellow curved rods represent *V. cholerae* cells. Red chains permeating through biofilm space represent exopolysaccharide. The biofilm-specific adhesion protein Bap1 anchors the biofilm cluster to abiotic surfaces, relying on a 57–amino acid loop (residues Tyr^{415}-Lys^{471}) with the sequence shown. Four pseudo repeats in the Bap1-57aa sequence are shown in blue, magenta, black, and red. The central aromatic-rich linker (WFFG) is shown in cyan, and the rest of the residues are shown in green. The core motif of the peptide is underlined. Bottom: Schematic representation of the peptide with the repeating units shown as rectangles with the corresponding colors and aromatic residues in the central linker shown as circles. Created in BioRender. J. Yan (2026; https://BioRender.com/1hhgjpq). (**B**) From left to right: microscopy images of the FITC-labeled Bap1-57aa peptide spontaneously adsorbing to surfaces of 5-μm silica beads, silica beads with amine groups on the surface (Silica-NH_2), PS beads with carboxylate groups on the surface (PS-COOH), and PS beads with nonionic surface coatings (PS-nonionic), respectively. Dextran (4 kDa) conjugated to FITC was used as a negative control. (**C**) Adsorption curves of the Bap1-57aa peptides on 5 μm beads with different chemistries. The excess intensity ($I_{ring} - I_{solution}$) was measured for each condition. The lipid adsorption curve was included for comparison. (**D**) Adsorption of peptide variants on various 5-μm beads. Shown are the excess intensity values measured at a peptide concentration of 4 μM. Core motif corresponds to a 10aa peptide; WFFG→LGPE corresponds to a 57aa peptide with the central linker WFFG swapped to LGPE; two-repeat corresponds to a peptide with only the first two pseudo-repeats. All data are depicted as means ± SD ($n = 3$). a.u., arbitrary unit.

a combination of fluorescence microscopy, molecular dynamics (MD) simulations, atomic force microscopy (AFM), lap shear tests, and spectroscopic tools. We reveal the molecular conformation and motifs of the peptide that underlie its surface association and further show that the peptide can efficiently glue microspheres together to form large precipitates, therefore acting as a flocculant.

RESULTS

Quantification of surface adsorption of the Bap1-57aa peptide

Figure 1A presents the sequence of the biofilm-derived peptide. The Bap1-57aa sequence is composed of four pseudo repeats, with a consensus sequence WbpKpnmY, where b, p, n, and m denote basic

Downloaded from https://www.science.org on November 20, 2026

(R, K, or H), polar (T, Q, or E), nonpolar (V or I), and mixed (P, A, or S) amino acids, respectively. Basic amino acids occur in two of the eight positions in the pseudo repeats, providing a rich possibility of hydrogen bonds and electrostatic interactions with abiotic surfaces. Aromatic amino acids appear twice in the repeats as well as in the linker, WFFG, between the two inner pseudo repeats.

To systematically quantify the surface adsorption of the Bap1-57aa peptide, we chemically synthesized the peptide with an N-terminal fluorescein isothiocyanate (FITC) label and measured its spontaneous adsorption onto microbeads using fluorescence microscopy (Fig. 1B) (*34*). In brief, beads (5 μm in diameter) with different compositions and surface properties were incubated with the FITC-labeled peptide and subsequently imaged with confocal microscopy (*43*). The biofilm-derived peptide spontaneously adsorbed onto a range of surfaces including silica and polystyrene (PS), showing a ring-like signal in the two-dimensional cross-sectional images. We also modified the surface chemistry of the beads using either silane chemistry or different PS sources. Bap1-57aa adsorption remained robust across these surface chemistries, highlighting its compatibility with diverse material interfaces and its potential for broad applications.

Subsequently, we generated adsorption curves of the Bap1-57aa peptide on different surfaces by measuring excess fluorescence signals on bead surfaces (I_{ring}, "ring" refers to the appearance of fluorescence on confocal images of peptide-bound beads) relative to the solution background ($I_{solution}$) at a series of peptide concentrations (Fig. 1C). The fluorescence signal on the beads is assumed to be proportional to the number of peptide molecules adsorbed on the surface. We generally observed a power law dependence at low peptide concentrations, followed by a plateau at high peptide concentrations, saturating at ~0.5 to 1 μM (M = mol/liter). Overall, the peptide exhibits similar levels of adsorption to PS and silica surfaces. Modifying the silica surface with amine (silica-NH_2) increases the adsorption by almost twofold, possibly due to aliphatic linkages between the amine group and the silica surface, which increase the surface's propensity for nonspecific adsorption, as can be seen in the dextran-FITC control (fig. S1). For this reason, we will pay less attention to adsorption results for the silica-NH_2 surface. For comparison, we have also included an adsorption curve on lipid-coated beads (*44*); binding to lipid bilayers is stronger than to abiotic surfaces, indicating that there are modes of interactions, such as membrane insertion, that are not possible on abiotic solid surfaces.

After establishing the binding assay, we sought to elucidate the surface-association mechanism of Bap1-57aa by designing and testing a series of peptide variants (Fig. 1D). Following our prior work on peptide-lipid binding (*44*), we studied the following set of mutants: (i) a short peptide with 10 amino acids corresponding to the "core motif" of the peptide (SYWFFGWHTK); (ii) a 57aa peptide with the central linker WFFG swapped to LGPE (WFFG→LGPE), preserving the contribution of the four pseudo-repeats while removing the effects of aromatic residues in the central linker; and (iii) a truncated peptide with only the first two pseudo-repeats (two-repeat; LGLEWKTKTVPYLGVEWRTKTVSY). The full amino acid sequences of these peptides can be found in fig. S2.

To simplify data interpretation, we measured and compared surface adsorption signals at a saturating concentration of 4 μM (Fig. 1D). For adsorption on the silica surface, the core motif contributes minimally, which may be related to the hydrophobic nature of the aromatic residues in the core motif and the hydrophilic nature of the silica surface. On the other hand, the pseudo-repeats appear to contribute additively to adsorption through avidity effects—increased binding strength through multiple affinities of individual noncovalent binding interactions (*45*). While the two-repeat sequence has no measurable adhesion (close to the negative controls), the WFFG→LGPE mutant with four pseudo-repeats shows an adsorption level similar to the counterpart of the wild-type (WT) Bap1-57aa peptide. Presumably, basic residues in the pseudo-repeats engage in electrostatic interactions with the negative charges on the silica surface. For adsorption on PS beads coated with either carboxylate groups or nonionic, hydrophilic stabilizers, both the core motif and the peripheral pseudo-repeats contribute to adsorption, albeit to different extents.

Overall, our data show that the biofilm-derived peptide can spontaneously adsorb to a range of surfaces. Mechanistically, the aromatic-rich core motif and the peripheral pseudo-repeats can both contribute to surface binding to varying degrees, depending on the surface chemistry.

Quantification of peptide-surface interactions with a quartz crystal microbalance

The fluorescence-based bead assay allowed us to make quantitative comparisons between variant peptides; however, it does not give us an absolute measurement of how many molecules are adsorbing onto the surface. Also, it is difficult to test the reversibility of the adsorption process in this assay. To address these limitations, we performed measurements of the WT peptide binding to silica surfaces using a quartz crystal microbalance with dissipation (QCM-D), a sensitive technique for quantitative measurement of surface adsorption and for assessing the reversibility of the adsorption process (*46*, *47*). A SiO_2 chip was initially rinsed with water and 0.7% (volume fraction) dimethyl sulfoxide (DMSO), then incubated with 1 μM peptide dissolved in 0.7% DMSO, and lastly rinsed with 0.7% DMSO, isopropanol, ethanol, and SDS solution (10 g/liter) (Fig. 2A). After each rinse, values in water were recorded again (Fig. 2, A and B). Frequency and dissipation were recorded in the third, fifth, seventh, and ninth harmonics, which had low variability (fig. S3).

The binding of the Bap1-57aa peptide to SiO_2 is largely irreversible, as the measured frequency when exchanged into pure water after peptide adsorption remained constant at ~−6.5 Hz compared to the initial value in water. Even after rinsing with isopropanol or ethanol, the measured frequency of the silica surface with peptide bound did not return to the initial value in water. This stable adsorption is useful for potential underwater applications. After rinsing with SDS, the frequency almost returned to zero, with an average value of (−0.3 ± 0.1) Hz, which is within the sensitivity of the instrument (1 Hz), suggesting that SDS removed most of the peptide from the surface.

We then repeated the experiment four times to assess consistency. The average frequency change in the fifth harmonic of the peptide layer on the surface for each experiment was (−6.7 ± 0.6), (−6.8 ± 0.1), (−4.1 ± 0.1), and (−5.6 ± 1.4) Hz, respectively (average ± SD). The expected sensitivity of the OpenNEXT QCMD instrument with 5-MHz sensors is 1 Hz (or equivalently 17.7 ng/cm^2). This allows us to estimate the expected signal from the peptide using the Sauerbrey relation (see Materials and Methods) (*48*) by assuming a complete, continuous monolayer of protein lying flat on the surface, homogeneous,

Downloaded from https://www.science.org on November 20, 2026

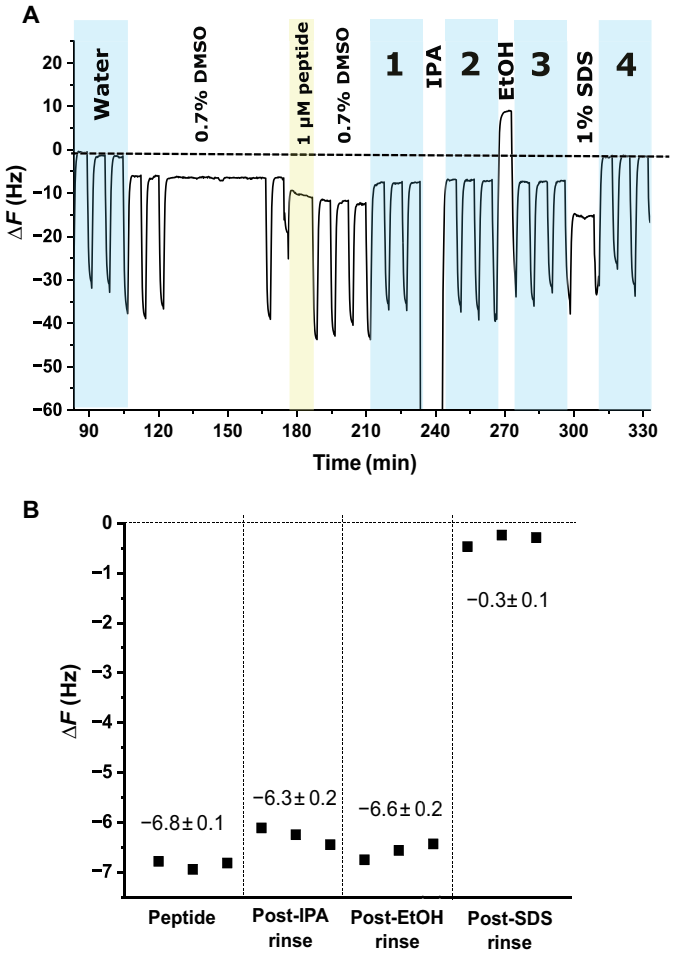


Fig. 2. Representative quartz crystal microbalance measurement of Bap1-57aa adsorption on a SiO_2 chip. (**A**) Changes in fifth harmonic frequency over time relative to the initial water injection. Sharp decreases in frequency are present at the time of injection, likely due to temperature variation upon injection. The yellow shading indicates where the peptide was injected. The dashed line represents the initial water value. Blue shading is used to denote measurements in water. The water measurements labeled 1, 2, 3, and 4 are plotted for clarity in B. (**B**) Difference in frequency for the SiO_2 chip in water after incubation with the peptide, rinsing with isopropanol (IPA), rinsing with ethanol (EtOH), and rinsing with SDS. The zero value was set to the average frequency for five measured water injections before incubation with peptide. The average of the three measurements is shown above the data points, with the error corresponding to the SD.

and isotropic. The thickness of this layer is estimated to be the size of an amino acid or 0.8 nm (*49*), assuming a linearly extended conformation of the peptide on the surface. The estimated density is that of protein, 1.2 g/cm^3. The mass per area is thus

$$\left(1.2\ \mathrm{g/cm^3}\right)\left(8\times10^{-8}\ \mathrm{cm}\right)=96\ \mathrm{ng/cm^2} \quad (1)$$

leading to an expected frequency change of −5.5 Hz for a complete monolayer of protein. The average frequency change for our four measurements was (−5.8 ± 1.3) Hz, which agrees with the expected value for a monolayer, corresponding to a 5% difference between the measurement and the theoretical estimate. We caution, however, that this estimate is based on many assumptions, particularly that the peptide homogeneously covers the silica surface. In practice, strong peptide-peptide interactions can cause aggregation and consequently a heterogeneous film.

A biofilm adhesion assay confirms the contributions of various motifs in Bap1-57aa

Previously, we showed that the Bap1-57aa peptide is critical for the proper adhesion of *V. cholerae* biofilms to abiotic surfaces using a biofilm adhesion assay (*34*). Here, we used the same assay to test some of the conclusions from the in vitro characterization (Fig. 3A). To do so, we first generated *V. cholerae* mutants containing various *bap1* constructs (*34*). We then grew mature biofilms of *V. cholerae* cells constitutively expressing mNeonGreen on glass surfaces, followed by vigorous washing. Last, we quantified the biomass on the glass before and after the wash and used the ratio between the two as an indication of adhesion strength. Biofilms possessing a WT 57aa sequence will have a value close to 1, whereas nonadhesive mutants, such as the 57aa deletion mutant (Δ*57aa*), will have a value close to 0. We used increasing concentrations of bovine serum albumin (BSA) as a competitive inhibitor of surface binding.

As shown previously, we verified that biofilms with a WT 57aa sequence robustly adhere to the glass surface regardless of the presence of BSA, while the negative control (the Δ*57aa* mutant) has minimal ability to adhere to glass (Fig. 3B). Next, we tested several 57aa variants with sequences that correspond to the peptides we have chemically synthesized and tested in the bead adsorption assay. Replacing the full 57aa sequence with the 10aa core motif significantly affects the adhesion ability (Fig. 3B, core motif): The corresponding mutant biofilm lost adhesion as BSA (0.2 mg/ml) was added. The mutant biofilm with the two-repeat peptide is similarly defective in this assay (Fig. 3B, two-repeat). The four-repeat variant (WFFG→LGPE) showed greatly improved glass adhesion compared to the two-repeat variant (Fig. 3B; WFFG→LGPE); however, unlike WT, the amount of biomass remaining decreases as BSA concentration increases in this strain, suggesting that its adhesive strength is lower than that of the WT biofilm. As an alternative method to test peptide-surface interactions in the biofilm context, we also visualized the spatial localization of Bap1 molecules in biofilms using a 3×FLAG tag combined with a fluorescent anti-FLAG antibody (*34*, *37*, *50*). While WT Bap1 signal concentrates underneath the biofilm, in all defective mutants, the Bap1 surface signals are significantly diminished, consistent with their reduced adhesive abilities (fig. S4). All these results are consistent with the observations in the in vitro bead adsorption assay.

We note a potential difference in the microenvironment of the Bap1-57aa peptide in the biofilm-based and in vitro assays: In the former, the 57aa is a loop nested in a well-folded domain, whereas in the latter, the Bap1-57aa peptide lacks end-to-end restraints. To test if this difference affects our conclusions, we constructed a mutant in which the 57aa sequence was repositioned at Bap1's C terminus, thus releasing the end-to-end restraints on the peptide. We found that this mutant has an intact ability to bind to the glass surface (Fig. 3B, C-terminal 57aa), suggesting that the 57aa peptide can function independently of its original loop context when adhering to glass, consistent with the in vitro results with chemically synthesized peptides that have no such conformational restraints.

MD simulations reveal the molecular mechanism of surface adsorption

To further understand the molecular mechanism underlying the surface association of the Bap1-57aa peptide, we performed all-atom

Downloaded from https://www.science.org on November 20, 2026

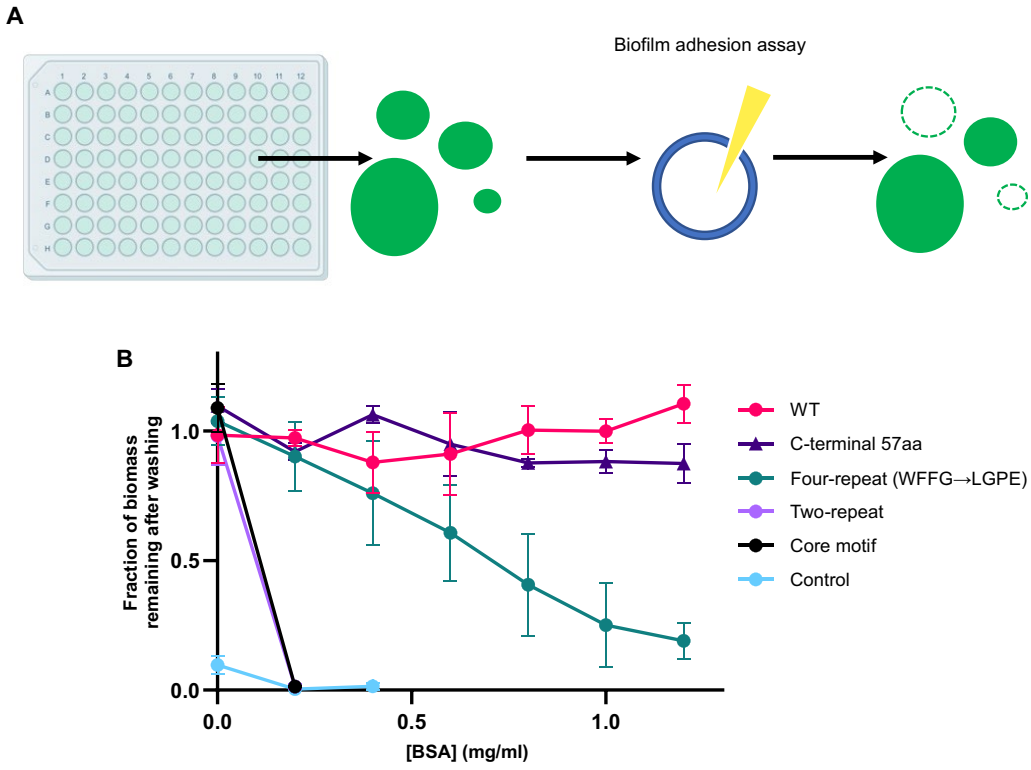


Fig. 3. Adhesive function of the Bap1-57aa peptide in the native biofilm context. (**A**) Schematic of the biofilm adhesion assay. Briefly, biofilms from *V. cholerae* cells constitutively expressing mNeonGreen and various *bap1* mutants were grown overnight and imaged with confocal microscopy. Subsequently, the biofilms were vigorously washed and imaged again at the same location. The fraction of biofilm biomass remaining on the substrate reflects the adhesive ability of the biofilms. Created in BioRender. J. Yan (2026; https://BioRender.com/lrdb9bf). (**B**) Results from the biofilm adhesion assay for different peptide variants. BSA was used at increasing concentrations during biofilm growth as a nonspecific competitor for glass surface adhesion. A Δ*57aa* strain was used as the negative control. All data are depicted as means ± SD ($n = 3$).

MD simulations of the peptide on a silica surface. Unlike our previous work on Bap1-57aa–lipid interactions (*44*), we expect that its interaction with the silica surface is largely electrostatic in nature, given the polar and negative charge characteristics of the surface. The Bap1-57aa peptide is enriched in charged residues, with eight positively charged residues (Lys and Arg) and three negatively charged residues (Glu), resulting in a net charge of +5 (Fig. 4A). The analysis of the contact frequencies of individual residues with the silica surface (with a 3.5-Å distance cutoff) shows that several positively charged [lysine (Lys) and arginine (Arg)] and polar [serine (Ser), tryptophan (Trp), and tyrosine (Tyr)] amino acids frequently form hydrogen bonds with the silica surface (Fig. 4, B and C).

To generate further insights, we divided the Bap1-57aa sequence into N-half (Tyr^{415}-Phe^{442}) and C-half (Trp^{444}-Lys^{471}), with each half containing two pseudo-repeats. Notably, the contact frequency analysis shows that the C-half interacts more strongly with the silica surface than the N-half (Fig. 4, B and C, top). Although the distribution of positively charged residues is equal in both halves of the peptide, the N-half contains two negatively charged Glu residues (Glu^{419} and Glu^{431}), whereas the C-half contains only one (Glu^{458}). Moreover, the repulsive effect of Glu^{458} in the C-terminal half is reduced because it is flanked by two positively charged Lys residues. In contrast, in the N-terminal half, Glu residues are not next to a positively charged residue.

The electrostatic interactions with the surface largely explain the surface adsorption abilities of different peptide variants (Figs. 1D and 3B): The WFFG→LGPE mutant largely retains the charge distribution of the WT Bap1-57aa sequence and hence has a similar or slightly reduced adsorption strength. The two-repeat peptide has a reduced avidity effect due to the reduced number of positive charges. Last, the core motif, although showing strong lipid association due to membrane insertion (*44*), has low contact frequencies with the silica surface and correspondingly performs worse when interacting with various solid surfaces compared to the WT peptide or the WFFG→LGPE mutant.

In addition to the key residues for surface association, the MD simulations revealed interesting conformational information (Fig. 4B). In our previous work on the Bap1-57aa–membrane interaction (*44*), we showed that in solution, the Bap1-57aa peptide forms a mixture of random coils and β sheets, which convert into a characteristic β-hairpin structure upon inserting into the hydrophobic core of lipid bilayers when encountering a membrane. In contrast, here, we found that, starting from a disordered conformation, several regions of the Bap1-57aa peptide, especially in the C-half, adopt a helical conformation with 35 to 65% probabilities upon interacting with the silica surface (Fig. 4C, bottom). The transition from a disordered state to helical formation is driven primarily by the tethering of the residues within (W456 and K457) and flanking (R433, Y463, and K471) the helical regions.

Collectively, these observations demonstrate that binding between the Bap1-57aa peptide and the silica surface is largely regulated by the spatial arrangement of positively and negatively charged residues and hydrogen bond–forming residues. Our results also highlight how an

Downloaded from https://www.science.org on November 20, 2026

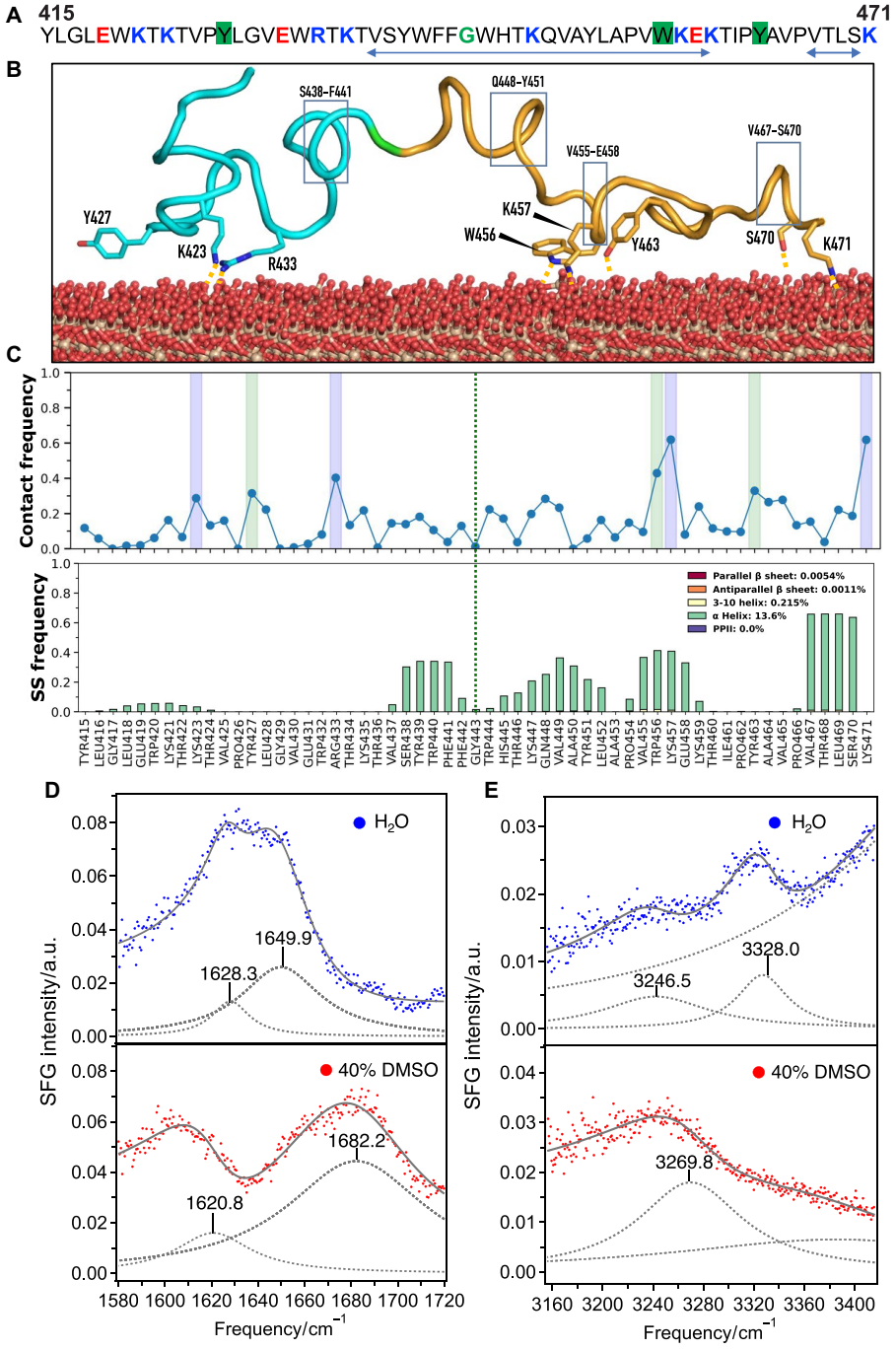


Fig. 4. Interaction of the Bap1-57aa peptide with silica surfaces induces helix formation, revealed by MD simulations and SFG spectroscopy. (**A**) Sequence of the Bap1-57aa peptide with aromatic residues involved in surface interactions highlighted by green shading, positively charged residues in blue, and negatively charged residues in red. The central residue Gly^{443} divides the Bap1-57aa peptide into N-half (Tyr^{415}-Phe^{442}) and C-half (Trp^{444}-Lys^{471}). The arrows indicate the regions of helix formation, mostly located in the C-half of the peptide. (**B**) A representative snapshot from MD simulations of the Bap1-57aa peptide on a silica surface showing contacts with negatively charged surface sites. Interacting residues Tyr^{427}, Lys^{423}, Arg^{433}, Trp^{456}, Lys^{457}, Tyr^{463}, Ser^{470}, and Lys^{471} are shown in stick representation. The N-half and C-half of the peptide are shown in cyan and orange cartoons, respectively. The silica surface is shown in sphere representation, with O and Si atoms colored red and orange, respectively. Regions with a helical conformation are highlighted with rectangles. (**C**) Top: Per-residue contact frequency with the silica surface within a 3.5-Å distance cutoff between peptide and silica heavy atoms. Ten independent simulations were performed. Bottom: Frequency of secondary structures (SSs) of the Bap1-57aa peptide for each residue from simulations starting from a disordered conformation. Average contact frequencies and SS are calculated from the last 500 ns of each replica, corresponding to a total of 5 μs of simulation time. (**D**) SFG spectra in the amide I region and (**E**) in the NH stretch region of the Bap1-57aa peptide deposited on a glass slide prepared using H_2O (top, blue) and 40% DMSO (bottom, red) as solvents. The spectral fitting is shown in solid gray lines with the fitting component peaks shown in gray dashed lines, where the fitted peak positions are marked in wavenumbers (cm^{-1}).

Downloaded from https://www.science.org on November 20, 2026

intrinsically disordered peptide can adopt different conformations when interacting with different surfaces.

Sum frequency generation spectroscopy confirms the helical conformation of the peptide on silica surfaces

Next, we sought to verify the α-helical conformation of the peptide when adsorbing on negatively charged silica surfaces, as predicted by the MD simulations. Since most spectroscopic techniques, such as circular dichroism, only give information of the molecular conformations in solution, we resorted to vibrational sum frequency generation (SFG) spectroscopy, a technique specifically sensitive to vibrational structures of molecules adsorbed at interfaces (*51*–*54*). In an SFG experiment, an infrared (IR) beam at frequency ω_{IR} and a visible beam at frequency ω_{vis} overlap temporally and spatially at the sample surface to generate SFG signals at the sum frequency ($\omega_{SFG} = \omega_{vis} + \omega_{IR}$). This optical process depends on the second-order susceptibility, $\chi^{(2)}$, which is zero in centrosymmetric media, such as bulk liquids. At interfaces, however, centrosymmetry is broken, leading to a nonzero $\chi^{(2)}$. As a result, SFG is sensitive to molecules adsorbed at interfaces. When applied to study proteins at interfaces, SFG can characterize secondary structures by probing the peptide backbone amide I and/or NH stretching modes (*51*, *52*, *54*). The amide I bands at lower frequencies (1620 to 1630 cm^{-1}) and/or higher frequencies (1680 to 1690 cm^{-1}) are indicative of β sheet structures, whereas amide I bands in the range of 1640 to 1660 cm^{-1} are characteristic of α helices. Moreover, the NH stretching frequencies are higher for α-helical structures compared to β sheet structures due to the weaker hydrogen bonds experienced by the NH groups in α helices (*52*, *54*–*56*).

To investigate the peptide conformation at the interface, we examined the secondary structures of the Bap1-57aa peptide deposited on a glass substrate. To illustrate the sensitivity of SFG to peptide secondary structures, we collected the amide I and NH spectra (Fig. 4, D and E) of the sample prepared using pure water and then repeated the experiments with the sample prepared using 40% DMSO (volume fraction). As the peptide dissolves more readily in DMSO than in pure water (*34*, *44*), we hypothesized that 40% DMSO will disrupt the surface-peptide interactions and perturb the peptide secondary structures. The SFG spectrum of the sample prepared using pure water (Fig. 4D, top) shows two peaks at (1628.3 ± 0.5) and (1649.9 ± 0.4) cm^{-1}, corresponding to β sheet and α-helical structures, respectively, with the latter showing a higher amplitude in the fitted result (dotted curves in Fig. 4D, top, and table S1). These peaks are not due to water OH bending modes, as they remain largely unchanged when H_2O is replaced by D_2O (fig. S5). The SFG spectrum of the sample prepared using 40% DMSO (Fig. 4D, bottom) shows significantly different amide I bands at (1620.8 ± 1.2) and (1682.2 ± 2.0) cm^{-1}, which are highly characteristic of β sheets (table S2). Figure 4E shows the NH spectra for the sample prepared using pure water (Fig. 4E, top), which exhibits peaks at (3246.5 ± 4.0) and (3328.0 ± 1.9) cm^{-1}, attributed to β sheet and α helix structures, respectively (table S1). Conversely, the sample prepared using 40% DMSO (Fig. 4E, bottom) shows a pronounced peak at (3269.8 ± 2.9) cm^{-1}, attributed to β sheet structures (table S2). These experiments clearly show that SFG is sensitive to the secondary structure of the Bap1-57aa peptide adsorbed on the glass surface. The results also reveal that the Bap1-57aa peptide, when first dissolved in water, adopts α-helical conformations on the glass surface with some contribution of β sheets (Fig. 4, D and E, and table S1). Because depositing proteins on solid substrates often induces protein aggregation yielding β sheet–rich structures (*57*), our observation of Bap1-57aa in α-helical structures is noteworthy and consistent with the MD simulations (Fig. 4C) highlighting the α-helical conformation near the glass substrate. Adding support to the importance of peptide conformation, we showed that a 57aa peptide with scrambled sequence generally binds less well to the surfaces tested (fig. S6B).

AFM and lap shear tests of the adhesive ability of the biofilm-derived peptide

Our characterization so far focused on the adsorption and conformation of the Bap1-57aa peptide. To evaluate its potential as an underwater adhesive, we performed a series of experiments using AFM to quantify the underwater adhesion strength of the biofilm-derived peptide (Fig. 5A). We have previously used this AFM-based method to measure adhesion of various mutant *V. cholerae* cells to determine the proteins involved in adhesion (*40*). Briefly, silica beads were first attached to tipless AFM cantilevers and subsequently coated with peptide by incubating with 4 μM peptide in water for >20 min. Next, the bead with adsorbed peptides was allowed to approach a pristine mica surface in water, and forces were measured. Upon retraction of the probe from the surface, the force-distance curves demonstrated a substantial adhesive force corresponding to the adhesion conferred by Bap1-57aa (Fig. 5A and fig. S7). From the force-distance curves, we extracted the maximum adhesive force or pull-off force. By repeating this measurement multiple times at multiple locations, we generated the distribution of pull-off forces for each peptide variant (Fig. 5B). We observed that the WT peptide shows the strongest pull-off force (11.5 nN), whereas both the core motif and the WFFG→LGPE variant show a more than threefold reduction in pull-off force. This observation is largely consistent with the adsorption data.

Using the Derjaguin-Muller-Toporov (DMT) relationship (*58*, *59*), $F = 2W\pi R$in which R is the bead radius (the nominal radius of curvature of the colloidal probes in this case) and W is the work of adhesion, we estimate W to be ~0.75 mJ/m^2. This value falls into the range of adhesive strengths measured for other underwater adhesive peptides/proteins (*60*). We also note that the procedure could be further optimized to increase W. For example, when varying the contact time after the beads come into contact with the mica substrates, we found that a short surface dwelling time (5 s) is helpful for proper adhesion (fig. S8); this could be related to the time needed for the peptide molecules to rearrange on the surface.

Complementing the microscale AFM measurements, we also performed lap shear measurements (*16*, *61*) to test the application potential of Bap1-57aa at the macroscopic scale. By sandwiching a Bap1-57aa solution at 8 mg/ml (≈1.2 mM) between two glass slides and allowing a brief contact time optimized for each condition, we measured the adhesion strength of the system while the sample was still wet. Typical stress-extension curves are shown in Fig. 5C, and statistics are shown in Fig. 5D. We used BSA solutions at the same mass concentrations for comparison. We observed that using the particular preparation procedure (see Materials and Methods), we indeed obtained an appreciable adhesion strength (>80 kPa) under wet conditions, particularly at high salinity concentrations relevant to brackish or oceanic water. The measured values are significantly higher than the BSA control and comparable to those measured for molecules designed based on Mfps at similar concentrations (*16*). We found that the measured strength is consistently higher in a salty solution than in deionized (DI) water, suggesting that electrostatic screening promotes the adhesive functions of peptide. This may be related to the stronger aggregation tendency of the peptide when

Downloaded from https://www.science.org on November 20, 2026

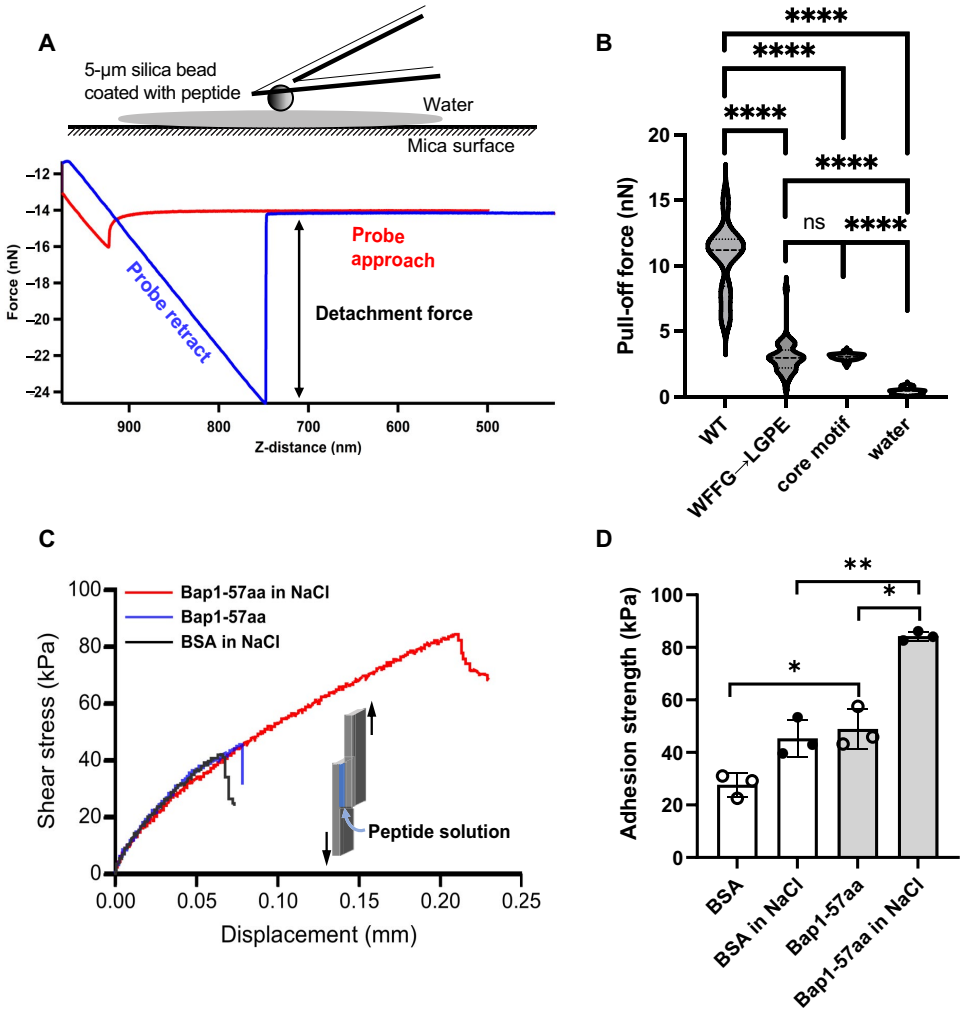


Fig. 5. AFM and lap shear test for characterizing the underwater adhesive strength provided by the biofilm-derived peptide. (**A**) Representative force-distance curve for the WT Bap1-57aa peptide in water. Inset: Schematic of the experimental setup. In brief, silica beads were first attached to the tip of AFM cantilevers, and subsequently coated with the peptide by incubating with 4 μM peptide in water. Next, the bead was allowed to approach a pristine mica surface in water and forces were measured. (**B**) Pull-off forces measured for the WT peptide, the WFFG→LGPE mutant, the core motif, and the water control (without any peptide), presented as violin plots. Dashed lines correspond to 75th percentile (third quartile), median, and 25th percentile (first quartile). All statistical analyses were performed using unpaired, two-tailed *t* tests with Welch's correction. ns, not significant (WFFG→LGPE v.s. core motif, $P = 0.7182$), ****$P < 0.0001$. WT, $n = 42$; core motif, $n = 42$; WFFG→LGPE, $n = 46$; water-only control, $n = 27$. (**C**) Typical stress-extension curves of lap shear measurements of Bap1-57aa in DI water and in 400 mM NaCl and BSA in 400 mM NaCl, all prepared at 8 mg/ml. Inset: Schematic of lap shear measurements for two glass slides adhered by a peptide solution. (**D**) Measured adhesion strength of Bap1-57aa at 8 mg/ml, in comparison to the BSA control, in DI water, and in 400 mM NaCl, respectively. All data are depicted as means ± SD ($n = 3$). All statistical analyses were performed using unpaired, two-tailed *t* tests with Welch's correction. *$P < 0.05$ (BSA versus Bap1-57aa, $P = 0.0219$; Bap1-57aa versus Bap1-57aa in NaCl, $P = 0.0118$) and **$P < 0.01$ (BSA in NaCl versus Bap1-57aa in NaCl, $P = 0.0081$).

electrostatically screened, which in turn may be due to a competition between the interpeptide attraction caused by hydrophobic residues and repulsion between the positively charged residues.

Potential application of the biofilm-derived peptide as a flocculant

During the fluorescence microscopy experiments performed in the bead-based adsorption assay, we observed that the Bap1-57aa peptide has a tendency to aggregate. Combining the aggregation tendency with the surface adsorption capability, we propose that the Bap1-57aa peptide may be used as a flocculating reagent to clear particulate contaminants from water. To demonstrate this point, we used well-dispersed suspensions of small (200 nm) PS particles as a model pollutant. The addition of FITC-labeled Bap1-57aa peptides to the particle suspension induced the formation of large coaggregates with an interconnected network of beads and peptides, decreasing the number of particles remaining in solution (Fig. 6A). While the peptides can aggregate alone at the same concentration, the morphology of the coaggregates is more compact; this suggests that while the peptide can bridge PS particles, the PS particles also help condense the protein aggregates. To generate mechanistic insights, we systematically increased the peptide concentration while keeping the bead concentration constant (Fig. 6B). At low peptide concentrations, most particles exist in free states (or settle on the

Downloaded from https://www.science.org on November 20, 2026

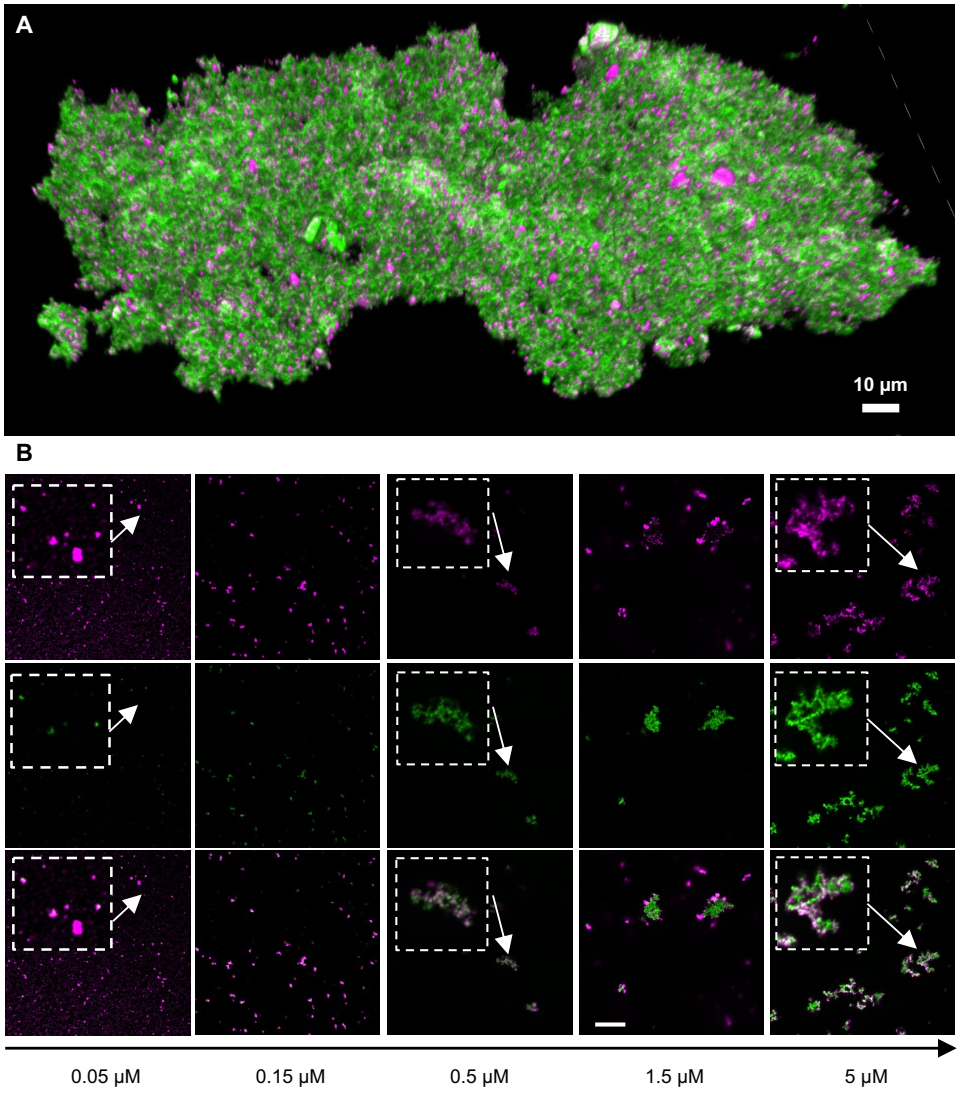


Fig. 6. Bap1-57aa peptide as a flocculant. (**A**) Three-dimensional view of a large aggregate formed by the FITC-labeled Bap1-57aa (3 μM, green) and 200-nm PS beads [2×10^{-4} weight % (wt %), magenta] in M9 solution containing BSA (0.2 mg/ml). (**B**) Cross-sectional view of suspensions in PBS solution containing 200-nm PS beads (5×10^{-3} wt %, magenta) and increasing concentrations of FITC-labeled Bap1-57aa. Shown from top to bottom are the bead channel, the peptide channel, and the overlay, respectively. Scale bar, 20 μm. Inset shows zoomed-in views for the highlighted region.

glass substrate), whereas the FITC signals from the peptide colocalize precisely with the bead signal due to surface adsorption. As the peptide concentrations increase, the size and number of the coaggregates increase while the number of free beads decreases (fig. S9A). At high peptide concentrations (>1 μM), most particles are associated with the coaggregates in contrast to the BSA control (fig. S9B), demonstrating the efficacy of the biofilm-derived peptide as a flocculant for particle removal.

DISCUSSION

In this study, we used a combination of characterization techniques including microscopy, spectroscopy, mechanical testing, and computer simulations to unravel the molecular mechanisms of surface adhesion of a biofilm-derived peptide. We find that the unique peptide originally discovered in the *V. cholerae* biofilm adhesin Bap1 uses multiple sequence features to interact with a range of abiotic surfaces ranging from silica to PS with various surface modifications. Using AFM and lap shear tests, we obtained a proof-of-concept demonstration that the peptide can be used to glue wet surfaces together both at the micron scale and at the macroscopic scale. This knowledge may open new avenues for developing bioinspired adhesives and biofilm control strategies.

The biofilm-derived peptide may offer several advantages over the popular design of bioadhesives inspired by Mfps. First, the absence of DOPA moieties means that it is chemically more stable and it can be applied in various aqueous environments. The simplicity in manipulating peptide sequences in bacteria also allows rapid testing and screening of optimized sequences for particular applications. Second, because of its bacterial origin and the absence of posttranslational modifications, it could be potentially mass-produced through fermentation, paving the way for scaling up its production for industrial

Downloaded from https://www.science.org on November 20, 2026

use. Third, computational tools for gaining insights into molecular level information on how environmental factors impact conformation, folding, or aggregation, are readily available for peptides and proteins based on canonical amino acids. Last, the sequence can be easily integrated into other recombinant proteins to direct a protein to adhere to desired surfaces.

Previously, we have shown that the Bap1-57aa peptide also binds strongly to lipid bilayers (*34*, *44*), which is likely what the peptide has evolved for in the biofilm context to enable *V. cholerae* cells to colonize various epithelial surfaces in animal hosts. The ability to bind to both lipid membranes and abiotic surfaces renders Bap1-57aa peptide suitable as a multifunctional adhesive (*34*). In real-world environments, many abiotic surfaces are also contaminated by organic residuals including lipids and proteins and therefore creating a complex interface (*62*). Going forward, one could leverage the ability of the Bap1-57aa to interact with both lipids and abiotic substrates to design multifunctional underwater glues that achieve strong adhesion under diverse challenging conditions. These adhesives could find widespread applications including binding wet surfaces, repairing tissues, stabilizing implants, or as priming agents to improve adhesion of subsequent protecting films for underwater infrastructure. The peptide sequence has been successfully integrated into chitosan-based polymers for the use of mucoadhesives recently (*63*). Fine-tuning of the peptide's sequence or secondary structures or integrating it into other functional domains could potentially broaden its utility as a versatile biomolecular tool.

The MD simulation and SFG results suggest that while electrostatic interactions largely dominate the association between the peptide and the negatively charged silica surface, the ability of the peptide to form α-helical structure on the silica surface to properly arrange the positively charged residues spatially is also potentially important. Our current data show that scrambling the sequence while maintaining the overall length and charge composition leads to lower adhesive function. However, when we scrambled two out of the four peripheral repeats, we did not observe a consistent trend (fig. S6C); more peptide mutants targeting the peptide secondary structure need to be synthesized and analyzed in the future. The optimization of the sequence will potentially lead to peptide adhesives with even better performance: It is unlikely that the WT sequence displayed by *V. cholerae* presents the optimal solution, and natural sequence variations in 57aa also exist (*44*, *64*). The performance of adhesives is affected not only by the ability of the peptide to adhere to surfaces but also the ability of the peptide to interact with other peptide molecules that defines the cohesive strength of the adhesive layer. In this regard, increasing the fraction of positive charges in the sequence will likely enhance surface adsorption but at the expense of peptide-peptide association and consequently the cohesive strength. A central question for future research is, therefore, how to balance adhesion and cohesion to achieve the best adhesive performance. Note that both adhesion and cohesion are affected by a range of environmental factors including ionic strength, nature of ions, pH, temperature, and surface properties including charge, hydrophobicity, and roughness (*65*). Particularly, in this study, we kept all solutions at pHs close to 7 for consistency and for biological relevance; the effect of pH on the conformation and adhesive behavior of the biofilm-derived peptides warrants further study in the future.

Our previous work using surface force apparatus (SFA) has provided quantitative measurement of the adhesive strength of Bap1-57aa, as well as the core motif, between two mica surfaces (*60*). In that study, under comparable conditions, the pull-off force measured by the peptide based on the sequence of the core motif is similar to or even higher than that measured for Mfps, particularly Mfp5, the Mfp with highest DOPA content (*11*). The different geometries, length scales, procedures, and rates at which the surfaces are displaced relative to each other in AFM and SFA may lead to the discrepancy in the results: In the SFA, prepared through a symmetric geometry, the core motif peptide generally performs better than the WT Bap1-57aa (*60*). In the AFM procedure presented here, the peptide molecules need to coat the beads surface first, which may explain why WT Bap1-57aa performs the best considering its stronger ability to adsorb onto the silica surface. Further work characterizing the film thickness, molecular arrangement and hysteresis, and morphology of the adhesive film may shed light on this difference and, more importantly, the failure mode during pull off.

Intrinsically disordered peptides or proteins (IDPs) have received much attention recently due to their ability to form membraneless organelles or condensates in cells (*66*–*69*). However, IDPs can also display transient secondary structures when interacting with other molecules (*68*, *70*). We found that Bap1-57aa displays different conformations when contacting different surfaces. Previously, using a combination of circular dichroism, fluorescence spectroscopy, and all-atom MD simulations (*44*), we have shown that the core motif (SYWFFGWHTK) forms a β-hairpin to insert into lipid membranes, while the peripheral repeating units increase lipid binding through avidity. On the other hand, the Bap1-57aa peptide assumes a mixture of β strands and random coils in solution and only turns into the β-hairpin conformation upon contacting lipids. Here, combining SFG measurement and MD simulations, we observed yet another conformation (largely α helix) when adsorbing on negatively charged silica surfaces. The flat energy landscape of IDPs allows facile conversion between conformations, which can be heavily influenced by an external surface. This principle could potentially be applied to the future design of peptide-based adhesives.

The ability to form coaggregates with solid particles not only enables the use of the biofilm-derived peptide as flocculant but also further opens the possibility of modifying its adhesive properties with particulate inclusions (*71*). In general, aggregation can be harnessed as a way for the mass production of adhesives, with potential to control aggregate structure, function, and size, by using solvent conditions as variables to tune dissipation pathways and to amplify the toughness of protein/peptide-based adhesives. For example, recently, Wilson *et al.* (*71*) chemically denatured BSA using urea to cause aggregation and developed an injection method for the mass production of underwater glues. Even cheaper proteins such as Zein (*61*) and soy proteins (*72*) have also been used with various denaturing methods for gluing wet surfaces such as water-soaked wood. Along this line, the mechanism underlying the aggregation tendency of the Bap1-57aa, as well as the contribution of the aggregation to adhesive function, warrants further mechanistic studies. Looking forward, the ability to produce the Bap1-57aa peptide from bacterial culture is critical for future applications on a large scale; we have preliminary data showing that this peptide can be obtained from *Escherichia coli* in a crude but functional form (fig. S10), but several technical issues during purification need to be solved, including how to remove impurities and avoid the use of surfactant for extraction.

MATERIALS AND METHODS

Source of materials

Chemically synthesized peptides are purchased from either Atlantic peptides or LifeTein. Results from the two sources are generally consistent. Polystyrene beads (5 μm) were purchased from Invitrogen

Downloaded from https://www.science.org on November 20, 2026

(nonionic, #N37460; sulfate, #S37227; carboxylate, #C37255). Silica beads were purchased from Polysciences (silica, #25348; silica-NH_2, #24758).

Bacterial strains

All *V. cholerae* strains used in this study were derivatives of the WT *V. cholerae* O1 biovar El Tor strain C6706str2 and listed in table S3. A rugose strain background was used, which harbors a missense mutation in the *vpvC* gene ($vpvC^{W240R}$) that elevates intracellular c-di-GMP levels (*73*). The rugose strains form robust biofilms and thus allow us to focus on the biochemical mechanisms governing surface binding rather than mechanisms involving gene regulation. For the biofilm adhesion assay, the other adhesin RbmC was further deleted to avoid confounding factors (*34*). For the matrix staining experiment, the functional copy of RbmC is present; otherwise nonadhesive biofilms will be washed away during the washing step. Moreover, all biofilm assays are performed in a Bap1 background in which the β-prism is deleted; previous work has shown that the cap of the β-prism contains several exposed lysine and tryptophan residues that confound the interpretation of the biofilm adhesion results (*34*). Additional mutations were genetically engineered into this *V. cholerae* strain using the natural transformation (MuGENT) method (*74*).

Bacterial growth

All strains were grown overnight in lysogenic broth (LB) at 37°C with shaking. 1× M9 salts were filter sterilized and supplemented with 2 mM $MgSO_4$ and 100 μM $CaCl_2$ (abbreviated as M9 medium below, pH = 7.0). Biofilm growth was generally performed in M9 medium supplemented with 0.5% glucose.

Bead-based adhesion assay

First, the surface of the 96-well plate was treated with NaOH to render it more hydrophilic and negatively charged. Briefly, before adding the solution, 100 μl of 10 M NaOH aqueous solution was added to the wells and incubated at room temperature for 10 min, after which the wells were washed with DI water until the pH was neutral. Chemically synthesized fluorescently labeled peptides (Atlantic or Lifetein peptides) were dissolved and stored in DMSO at 150 μM. A 100 μl of water containing BSA (1 mg/ml), various concentrations of FITC-labeled peptide or dextran-FITC, and 0.01% (weight percent) 5-μm microspheres was shaken in Eppendorf tubes for 1 hour at room temperature. The sample was then spun down and resuspended in 10 mM tris buffer (pH 7.4) and 150 mM NaCl before transferring to a NaOH-treated 96-well plate with a glass bottom (MatTek P96G-1.5-5-F) and allowed to settle at room temperature for 5 min before imaging. Thus-prepared samples were imaged with a spinning disk confocal microscope (Nikon Ti2-E connected to Yokogawa W1) using a 60× oil objective (numerical aperture = 1.40) and a 488-nm laser excitation and bright field. For each sample, at least three locations were imaged and captured with a scientific complementary metal-oxide semiconductor (sCMOS) camera (Photometrics Prime BSI). Each field of view contained roughly 100 to 150 beads.

Quantification of bead adsorption assay

The background signal due to the camera in the 488-nm channel was measured by taking images of M9 medium and quantifying them with built-in functions of the Nikon Element software. After subtracting the background signal, the signal intensity per unit area on the surface of the beads and in the solution was calculated using custom MATLAB codes, and the difference was determined to give the excess surface signal.

Quartz crystal microbalance

Wrapped silicon oxide sensors (5 MHz, 14 mm) from AWSensors (AWS SNS 000049 A) were used fresh from the package within 1 week of opening the package. No additional cleaning was performed, as directed by the supplier. Frequency at the overtones 15, 25, 35, and 45 MHz was monitored using the OpenQCM Next device. Data reported in Fig. 2 and in the main text are from the fifth (25 MHz) harmonic, although the results were the same within error across all overtones. Dissipation was also monitored at all overtones and remained low (<5 parts per million difference between water and water with the peptide film present) for the duration of the experiment, indicating that mass can be calculated using the linear Sauerbrey relationship with frequency change (*48*, *75*)

$$\Delta m = C\,\Delta F \tag{2}$$

in which C is the mass sensitivity constant of the quartz crystal. For our 5-MHz quartz sensors, $C = -17.7\ \mathrm{ng{\cdot}cm^{-2}{\cdot}Hz^{-1}}$. Peptide solutions were prepared by diluting 150 μM stock in DMSO into ultrapure water. For 1 μM peptide, the final DMSO concentration was ≈0.7% (volume fraction). This amount of DMSO was found to change the frequency compared to water, so values reported in Fig. 2 are in pure water, since little to no peptide washed off with each water injection. Water, isopropanol, and 0.7% DMSO were injected into the device before adding peptide to rinse the system and measure baseline values for water. In one experiment, the chip was washed with water, ethanol, and isopropanol before measuring the value of two water injections for 40 s each. After 1 μM peptide was injected, the chip was washed with subsequent water, 50 mM tris (pH = 7.4) and 100 mM KCl, water, isopropanol, and again water. Results obtained are similar to the other three datasets.

Biofilm adhesion assay

Overnight cultures of the indicated strains constitutively expressing mNeonGreen were grown from individual colonies at 37°C with shaking in 1.5 ml of LB. A 50 μl from each culture was used to inoculate 1.5 ml of M9 medium supplemented with 0.5% glucose and grown at 30°C with shaking until the optical density at 600 nm (OD_{600}) was between 0.1 and 0.3. The cultures were then diluted to an $OD_{600} \cong 0.001$. A 100 μl of the regrown culture was aliquoted into the wells of a 96-well plate with a glass bottom (MatTek P96G-1.5-5-F) and incubated at 30°C for 1 hour. The wells were then washed twice with M9 medium and replaced with M9 medium with 0.5% glucose and BSA (0, 0.2, 0.4, 0.6, 0.8, 1, or 1.2 mg/ml). The lid was secured with a layer of parafilm and the 96-well plate was subsequently incubated at 30°C for 16 hours. Thus-prepared samples were imaged with a spinning disk confocal microscope (Nikon Ti2-E connected to Yokogawa W1) using a 60× water objective (numerical aperture = 1.20) and a 488-nm laser excitation. For each sample, several locations with 3 by 3 tiles where imaged and captured with an sCMOS camera (Photometrics Prime BSI). The x-y pixel size was 0.22 μm, and the z-step size was 3 μm. The wells were then washed twice with M9 medium and reimaged at the same locations. All images presented in this study are raw data rendered using the Nikon Elements software.

Downloaded from https://www.science.org on November 20, 2026

Quantification of biofilm adhesion assays

Image analysis was performed with built-in functions of the Nikon Elements software by thresholding each image layer-by-layer and measuring the total binarized area above the threshold in each layer. The binary area for each sample *z*-slice was then summed to give the total biovolume, and the ratio of the total biovolume after versus before the washing step was calculated.

In situ biofilm immunostaining

Overnight cultures of the indicated strains with *bap1* tagged with 3×FLAG at the C-terminal and constitutively expressing mNeonGreen were grown following the same procedure as described above. The initial incubation time was adjusted to 30 min when biofilms were grown in the presence of BSA. The wells were washed twice with M9 medium; subsequently, 100 μl of M9 medium with 0.5% glucose, BSA (0.5 mg/ml; Sigma-Aldrich, A9647), and anti-FLAG antibody conjugated to Cy3 (2 μg/ml; Sigma-Aldrich, A9594) was added to the well. The lid was secured with a layer of parafilm and incubated at 30°C for 40 hours. Thus-prepared samples were imaged with a spinning disk confocal microscope (Nikon Ti2-E connected to Yokogawa W1) using a 100× oil immersion objective (numerical aperture = 1.35) or a 60× water immersion objective (numerical aperture = 1.20) and a 488-nm laser excitation to observe the cells and a 561 nm laser excitation to observe protein localization, with the corresponding filters. The images were captured with an sCMOS camera (Photometrics Prime BSI) at a *z*-step size of 0.5 μm.

Molecular dynamics simulations

To examine the binding behavior of Bap1-57aa on an abiotic silica surface, silica (α-Quartz) slab with dimension of 100 Å by 100 Å by 10 Å was constructed at neutral pH = 7 using nanomaterial modeler in the CHARMM-GUI web server (*76*) and solvated with a water box of 100 Å by 100 Å by 160 Å. A disordered structure of the Bap1 peptide (Tyr^{415}-Lys^{471}; 57 amino acids) was generated using TraDES (*77*) and placed near the silica surface. Overlapping water molecules within 1.5 Å of the peptide in the combined system (peptide + silica slab) were removed to avoid steric clashes. Na^+ and Cl^- ions were added to neutralize the system, and the ionic strength of the system was maintained to 150 mM NaCl. The total number of atoms was 156,124, including 47,567 water molecules. Silica force fields integrated into CHARMM were used for the SiO_2 nanomaterials (*78*). CHARMM36m (*79*) and TIP3P water model (*80*) force field were used for protein and water, respectively.

All simulations were performed using NAMD 3.0 (*81*). System was energy minimized for 10,000 cycles using the conjugate gradient and subsequently equilibrated at constant NVT (constant temperature and volume) for 250 ps with a 2-fs timestep. Positional restraints were applied to the heavy atoms of silica surface, while harmonic restraints were imposed on the protein backbone with a force constant of 10 kcal mol^{-1} $Å^{-2}$. Three successive equilibrations at constant NPT (constant temperature and pressure) simulations were performed for 1, 4, and 20 ns with 2-fs timestep, during which a force constant on the protein backbone was gradually reduced to 5, 2, and 1 kcal mol^{-1} $Å^{-2}$, respectively. Last, production simulations were performed for 0.6 μs in 10 replicates at constant NPT. Snapshots were saved at 100-ps interval, and the last 500 ns of each trajectory was considered for further analysis.

Long-range electrostatic interactions were treated using the particle mesh Ewald (PME) method (*82*). All bonds involving hydrogen atoms were constrained with the SHAKE algorithm (*83*). Nonbonded interaction cutoff was set to 12-Å cutoff with force switching starting at 10 Å. The temperature was maintained at 300 K using a Langevin thermostat with a damping coefficient of 1 ps^{-1}, and the pressure was controlled at 1 atm using the Nosé-Hoover Langevin piston method (*84*).

Analysis of simulation data

CPPTRAJ (*85*) and in-house Python scripts were used to calculate averaged secondary structure frequency for 10 replicate simulations. Contact frequency within 3.5-Å cutoff between heavy atoms and silica surface was calculated using tcl script in VMD (*86*) for each simulation and averaged over replicate simulations.

Sample preparation for SFG experiments

The Bap1-57aa peptide was added to pure water at 20 μM and sonicated for two intervals of 3 min for dissolution. Then, 20 μl of the sonicated solution was added onto a clean glass surface and allowed to dry overnight in a desiccator to form a film for the SFG experiments. Two other samples were prepared using the same procedures by replacing H_2O with D_2O or 40% DMSO as the solvent.

SFG spectrometer setup and data acquisition

A home-built broad bandwidth SFG spectrometer was used to collect SFG spectra with the *ssp* polarization (*s*-polarized SFG, *s*-polarized visible, and *p*-polarized IR beams). The experimental setup and the protocols used to collect and process SFG data were described in detail in previous work (*87*, *88*). In this study, SFG spectra were recorded for 10 min. The IR beam was tuned to the vibrational regions corresponding to the amide I and NH stretching regions for probing protein secondary structures. The resulting spectra were fitted into the Lorentzian line shape

$$I_{SFG} = \left| \chi^{(2)}_{NR} + \sum_q \frac{A_q}{\omega_{IR} - \omega_q + i\Gamma_q} \right|^2 \quad (3)$$

where I_{SFG} is the SFG intensity; $\chi^{(2)}_{NR}$ is the nonresonant contribution of the second-order susceptibility, ω_{IR} is the incident IR frequency, A_q is the amplitude, ω_q is the resonant frequency, and Γ_q is the damping factor for the qth vibrational mode. Error bars for the fitted parameters were computed in the data analysis software Igor Pro (version 9.01), with each error bar representing ±1 SD estimated from the fit residuals and covariance matrix, assuming normally distributed residuals.

Atomic force microscopy

AFM probes for adhesion measurement were prepared as described previously (*40*, *89*). Silica microspheres (Polysciences, Warrington, PA) with a diameter of 5.0 μm were attached to tipless AFM cantilevers (PNP-TR-TL-Au, NanoWorld, Switzerland) using ultraviolet curable optical adhesive (NOA 61, Norland Products). The probes were immersed in water containing 4 μM peptide for 20 min and then replaced with Milli-Q water. Force spectroscopy was performed with Asylum Cypher ES atomic force microscope. Probe calibration and spring constant determination were achieved via the thermal noise method. Curves were generated using a constant approach and retraction velocity of 0.5 μm/s. A retraction was triggered upon applying a 1 nN force following a 0- or 5-s dwell on the surface. Each force curve was analyzed individually in Igor Pro software. The adhesion force was taken to be the difference between the minimum and baseline

Downloaded from https://www.science.org on November 20, 2026

forces in the retraction curve. Multiple measurements were performed with the same probe at different locations; to compensate for the loss of peptide on the probe, we regenerated the probe by resoaking the probe in the peptide solution after repeated measurements when the probe fails to give proper signals. Force curves that did not show a clear adhesion event were excluded from the analysis. Forty-two force curves for WT, 42 force curves for core motif, 46 force curves for WFFG→LGPE, and 27 force curves for water only control were obtained with 5-s dwell for analysis. Thirty force curves for WT were obtained with 0-s dwell.

Lap shear test

In the lap shear experiments, hydrophilic glass surfaces were used as the substrates to evaluate the adhesion performance of chemically synthesized Bap1-57aa. The glass slides were cleaned by sonication in acetone for 10 min, followed by extensive rinsing with water and drying under a nitrogen stream. To prepare the specimens, 5 μl of the peptide/protein solution (Bap1-57aa or BSA) at a concentration of 8 mg/ml was applied onto a predefined 1 cm–by–1 cm area at the center of one glass substrate. The peptide/protein was dissolved in either DI water or a 400 mM NaCl solution (pH = 6.7). The solution was evenly spread across the 1 cm^2 bonding area using a pipette tip. A second glass slide was then overlapped to form the lap joint. During assembly, moderate rubbing and pressing were applied manually to ensure the formation of a uniform, thin film and to eliminate any trapped air bubbles. The assembled specimens were allowed to equilibrate for 3 min before testing: at room temperature for samples in 400 mM NaCl solutions and at 55°C for samples in DI water; we found that such a procedure provides optimal performance for each condition. All lap shear tests were performed using an Anton Paar MCR Rheometer (502WESP) equipped with a highly sensitive normal force (F_N) sensor. The bonded specimens were mounted on the rheometer stage using the accessory #129538 (solid torsion bar fixture SRF12/CTD V2.0), and the adhesion strength was measured in a pull-off mode with a constant separation speed of 150 μm/s. The adhesion strength was determined by dividing the peak detachment force (the absolute value of the maximum F_N recorded) by the bonded overlap area (1.0×10^{-4} m^2). Each condition was tested with at least three independent replicates, and the results are expressed as mean ± SD.

Bap1-57aa expression and extraction from *E. coli*

Bap1-57aa peptide expression and extraction was performed in a similar manner as previously described for Bap1 protein (*90*). DNA sequence of the 57aa, located within the β-prism domain of Bap1, was cut out and inserted into pET28b(+) using NdeI and XhoI restriction sites to generate a N-terminally His-tagged construct containing a thrombin cleavage site. The resulting sequence is: MGHHHHHHSSGLVPRGSHMDYLGLEWKTKTVPYLGVEWRTKTVSYWFFGWHTKQVAYLAPVWKEKTIPYAVPVTLSK. This construct was transformed into T7 Express *E. coli* (New England Biolabs), and overnight cultures were diluted 60-fold into fresh LB-Miller media (MP Biomedicals) supplemented with kanamycin monosulfate (50 μg/ml; GoldBio). Cultures were incubated at 37°C with shaking at 200 rpm until reaching an OD_{600} between 0.5 and 0.8. Protein expression was induced by the addition of 1 mM isopropyl its isopropyl-β-D-thiogalactopyranoside (GoldBio), followed by an additional incubation for 4 hours at 37°C with shaking at 200 rpm. Cells were pelleted by centrifugation in a Sorval LYNX 6000 centrifuge using an F9-6X-1000 LEX rotor at 5422*g* for 15 min at 4°C. Cell pellets were resuspended in 1× TBS [20 mM tris (pH = 7.5) and 150 mM NaCl] to a final volume of ≈10 ml per pellet from 1 L of expression culture. Samples were stored at −80°C until further processing. Thawed cell suspensions were supplemented with 1 mM protease inhibitor 4-(2-aminoethyl)benzenesulfonyl fluoride hydrochloride (GoldBio) and lysed via passage five times through an EmulsiFlex-C5 high-pressure homogenizer (Avestin Inc.) at ≈18,000 psi (124.1 MPa). The cell lysate was divided into two equal batches that were simultaneously centrifuged in a Sorvall LYNX 6000 at 21,734*g* for 30 min using an F20-12X50 rotor and further purified.

After centrifugation, the supernatant was discarded by decantation, and the pellet was resuspended by vortexing in 5 ml of detergent wash buffer [2× critical micelle concentration (CMC) of 3-[(3-cholamidopropyl)-dimethylammonio]-2-hydroxy-1-propane sulfonate in 1× TBS] per pellet from 1 L of expression culture. Resuspended pellets were stirred on a magnetic stirrer on ice for 30 min and centrifuged in a Sorvall LYNX 6000 at 21,734*g* for 30 min using an F20-12X50 rotor. Pellet resuspension was repeated with four different buffers: high salt wash buffer (1 M NaCl and 1× TBS), deoxyribonuclease (DNase) wash buffer [10 mM $CaCl_2$ and DNase I (up to ≈100 μg/ml)], 1× TBS wash buffer [20 mM tris (pH = 7.5) and 150 mM NaCl] and solubilization buffer [4× CMC $C_{12}E_8$ (octaethylene glycol monododecyl ether) and 1× TBS], respectively. All buffers were filtered using a 0.22-μm filter. Pellets resuspended in the solubilization buffer were subsequently stirred at room temperature. The soluble fraction (supernatant) containing Bap1-57aa peptide was stored at room temperature and the insoluble fraction (pellet) was stored at 4°C.

Gel electrophoresis (SDS-PAGE)

Samples were analyzed by SDS–polyacrylamide gel electrophoresis (SDS-PAGE) using gels prepared with 15% bisacrylamide (Bio-Rad), 25 mM tris (pH = 8.3), 0.05% ammonium persulfate (Thermo Fisher Scientific), and 0.025% TEMED (Bio-Rad). Electrophoresis was conducted at 180 V for 1 hour at room temperature in a running buffer composed of 25 mM tris, 192 mM glycine, and 1% SDS (pH = 8.35). Following electrophoresis, gels were stained overnight with 0.02% Coomassie Brilliant Blue G-250 in 10% acetic acid and subsequently destained in 10% acetic acid using Precision Plus Unstained Protein Standards (Bio-Rad) as the ladder. In another set of experiments, gels were used for transfer to polyvinylidene difluoride (PVDF) membrane; in these cases, Precision Plus Dual Color Protein Standards (Bio-Rad) were used as the ladder.

Western blot

Protein transfer to PVDF membrane was carried out at 100 V for 1 hour with an ice bag on the magnetic stirrer. Transfer buffer consisted of 25 mM tris and 192 mM glycine (pH = 8.3) and was incubated at −20°C for 20 min. After the transfer, the PVDF membrane was washed four times with 1× PBS-T buffer [137 mM NaCl, 2.68 mM KCl, 10.15 mM Na_2HPO_4, 1.76 mM KH_2PO_4, 0.05% (volume fraction) Polyoxyethylenesorbitan, and monolaurate (Tween 20) (pH = 7.4)] at 5-min intervals with shaking at room temperature. The membrane was subsequently blocked with lyophilized milk dissolved in 1× PBS-T buffer for 2 hours with shaking at room temperature, followed by three times of washing with 1× PBS-T buffer at 5-min intervals with shaking at room temperature. Next, the membrane was incubated overnight with goat anti-mouse immunoglobulin G (H + L–horseradish peroxidase conjugate) (Bio-Rad) primary antibodies with shaking at 4°C, followed by three times of washing with 1× PBS-T buffer at 5-min

Downloaded from https://www.science.org on November 20, 2026

intervals with shaking at room temperature. Subsequently, the membrane was incubated with 6×His Tag Monoclonal Antibody (HIS.H8, Invitrogen) secondary antibodies for 1 hour with shaking at room temperature, followed by three times of washing with 1× PBS-T buffer at 5-min intervals with shaking at room temperature. Last, the membrane was developed using Opti-4CN Substrate Kit (Bio-Rad), followed by washing in deionized autoclaved water for 15 min at room temperature without shaking.

Coaggregation assay

Ninety-six–well glass plate was treated with NaOH by adding 100 μl of 10 M NaOH to each well and incubating for 10 min. After the incubation, the NaOH solution was removed, and each well was washed six times with 200 μl of DI water, and the plate was left dry. Chemically synthesized Bap1-57aa peptide labeled with FITC was dissolved in DMSO and diluted to concentrations of 0.015, 0.05, 0.15, 0.5, 1.5, and 5 μM. To each sample, 200-nm FluoroSpheres carboxylate-modified beads (Invitrogen, # F8807) was added to a final concentration of 0.005% in 1× PBS buffer in a final volume of 50 μl. Negative controls with beads only and peptide only (at a concentration of 1.5 μM) were also prepared. Each sample was briefly vortexed, covered with aluminum foil, and incubated on a shaker for 1 hour. After the incubation, thus-prepared samples were transferred to the 96-well plate and imaged with a spinning disk confocal microscope (Nikon Ti2-E connected to Yokogawa W1) using a 60× oil objective (numerical aperture = 1.40). A 488-nm laser excitation was used to image the peptide, and a 640-nm laser excitation was used to image the PS beads, with the corresponding filters. For each sample, at least six locations were imaged and captured with an sCMOS camera (Photometrics Prime BSI), from which a representative image was shown for each condition in the figures.

Bap1-57aa peptide obtained from *E. coli* using solubilization buffer (4× CMC $C_{12}E_8$ in 1× TBS) was diluted to concentrations of 1.5, 5, 10, 25, 50, 100, 200, and 400 μM. To each sample, 200-nm FluoroSpheres carboxylate-modified beads (Invitrogen, # F8807) was added to a final concentration of 0.005% in 1× PBS to a final volume of 50 μl. Also added to the solution was 50× diluted NanoOrange (Thermo Fisher Scientific, N6666) to stain the peptide. Negative controls with beads only and peptide only (at a concentration of 50 μM, with and without NanoOrange) were also prepared. Each sample was briefly vortexed, covered with aluminum foil and incubated on a shaker for 1 hour. After the incubation, thus-prepared samples were transferred to the 96-well plate and subsequently imaged using the same setting as above.

Statistics and reproducibility

Error bars correspond to SDs from measurements taken from distinct samples unless indicated otherwise. Standard *t* tests were used to compare treatment groups and are indicated in each figure caption. All statistical analyses were performed using GraphPad Prism software. Microscopy images and spectra were shown from representative results from at least three independent experiments.

Supplementary Materials

The PDF file includes:

Figs. S1 to S10
Tables S1 to S3
Legend for data S1

Other Supplementary Material for this manuscript includes the following:

Data S1

REFERENCES

1. J. Yu, R. Xie, M. Zhang, K. Shen, Y. Yang, X. Zhao, X. Zhang, Y. Zhang, Y. Cheng, Molecular architecture regulation for the design of instant and robust underwater adhesives. *Sci. Adv.* **9**, eadg4031 (2023).
2. H. Fan, J. P. Gong, Bioinspired underwater adhesives. *Adv. Mater.* **33**, 2102983 (2021).
3. H. Ren, Z. Zhang, X. Cheng, Z. Zou, X. Chen, C. He, Injectable, self-healing hydrogel adhesives with firm tissue adhesion and on-demand biodegradation for sutureless wound closure. *Sci. Adv.* **9**, eadh4327 (2023).
4. J. H. Waite, M. L. Tanzer, Polyphenolic substance of *Mytilus edulis*: Novel adhesive containing L-dopa and hydroxyproline. *Science* **212**, 1038–1040 (1981).
5. B. K. Ahn, S. Das, R. Linstadt, Y. Kaufman, N. R. Martinez-Rodriguez, R. Mirshafian, E. Kesselman, Y. Talmon, B. H. Lipshutz, J. N. Israelachvili, J. H. Waite, High-performance mussel-inspired adhesives of reduced complexity. *Nat. Commun.* **6**, 8663 (2015).
6. E. W. Danner, Y. Kan, M. U. Hammer, J. N. Israelachvili, J. H. Waite, Adhesion of mussel foot protein Mefp-5 to mica: An underwater superglue. *Biochemistry* **51**, 6511–6518 (2012).
7. B. P. Lee, P. B. Messersmith, J. N. Israelachvili, J. H. Waite, Mussel-inspired adhesives and coatings. *Annu. Rev. Mater. Res.* **41**, 99–132 (2011).
8. J. Yu, Y. Kan, M. Rapp, E. Danner, W. Wei, S. Das, D. R. Miller, Y. Chen, J. H. Waite, J. N. Israelachvili, Adaptive hydrophobic and hydrophilic interactions of mussel foot proteins with organic thin films. *Proc. Natl. Acad. Sci. U.S.A.* **110**, 15680–15685 (2013).
9. H. Geng, P. Zhang, Q. Peng, J. Cui, J. Hao, H. Zeng, Principles of cation–π interactions for engineering mussel-inspired functional materials. *Acc. Chem. Res.* **55**, 1171–1182 (2022).
10. M. A. Gebbie, W. Wei, A. M. Schrader, T. R. Cristiani, H. A. Dobbs, M. Idso, B. F. Chmelka, J. H. Waite, J. N. Israelachvili, Tuning underwater adhesion with cation–π interactions. *Nat. Chem.* **9**, 473–479 (2017).
11. Q. Guo, J. Chen, J. Wang, H. Zeng, J. Yu, Recent progress in synthesis and application of mussel-inspired adhesives. *Nanoscale* **12**, 1307–1324 (2020).
12. F. Liu, X. Liu, F. Chen, Q. Fu, Mussel-inspired chemistry: A promising strategy for natural polysaccharides in biomedical applications. *Prog. Polym. Sci.* **123**, 101472 (2021).
13. M. D. Rivard, M. Renner-Rao, N. Hassanpour, F. Jehle, C.-S. Wang, D. A. Pham, D. J. Jackson, X. Banquy, M. J. Harrington, Proteins, processing, and properties of adhesive fluid condensates purified from mussels. *Adv. Funct. Mater.* **36**, e23693 (2025).
14. E. Filippidi, T. R. Cristiani, C. D. Eisenbach, J. H. Waite, J. N. Israelachvili, B. K. Ahn, M. T. Valentine, Toughening elastomers using mussel-inspired iron-catechol complexes. *Science* **358**, 502–505 (2017).
15. B. D. B. Tiu, P. Delparastan, M. R. Ney, M. Gerst, P. B. Messersmith, Enhanced adhesion and cohesion of bioinspired dry/wet pressure-sensitive adhesives. *ACS Appl. Mater. Interfaces* **11**, 28296–28306 (2019).
16. X. Ou, B. Xue, Y. Lao, Y. Wutthinitikornkit, R. Tian, A. Zou, L. Yang, W. Wang, Y. Cao, J. Li, Structure and sequence features of mussel adhesive protein lead to its salt-tolerant adhesion ability. *Sci. Adv.* **6**, eabb7620 (2020).
17. M. Cui, X. Wang, B. An, C. Zhang, X. Gui, K. Li, Y. Li, P. Ge, J. Zhang, C. Liu, C. Zhong, Exploiting mammalian low-complexity domains for liquid-liquid phase separation–driven underwater adhesive coatings. *Sci. Adv.* **5**, eaax3155 (2019).
18. C. R. So, E. A. Yates, L. A. Estrella, K. P. Fears, A. M. Schenck, C. M. Yip, K. J. Wahl, Molecular recognition of structures is key in the polymerization of patterned barnacle adhesive sequences. *ACS Nano* **13**, 5172–5183 (2019).
19. K. A. Ganar, M. Nandy, P. Turbina, C. Chen, D. Suylen, E. Nihoul, E. L. Pascoe, S. van der Beelen, M. Plaum, L. van den Bos, C. J. M. Koenraadt, I. Dijkgraaf, S. Deshpande, Phase separation and ageing of glycine-rich protein from tick adhesive. *Nat. Chem.* **17**, 186–197 (2025).
20. J. L. Clarke, P. A. Davey, N. Aldred, Sea anemones (*Exaiptasia pallida*) use a secreted adhesive and complex pedal disc morphology for surface attachment. *BMC Zoology* **5**, 5 (2020).
21. H. Lee, Y. Ryu, Y. Oh, C. Kim, Y. Lee, H. Choi, J. Kim, J. H. Kim, J. Kang, K. Park, K. T. Turner, S. Yang, H. Yoon, Starfish-inspired tube feet for temporary and switchable underwater adhesion and transportation. *Sci. Adv.* **11**, eadx3539 (2025).
22. F. Zeng, J. Wunderer, W. Salvenmoser, T. Ederth, U. Rothbächer, Identifying adhesive components in a model tunicate. *Philos. Trans. R. Soc. Lond. B Biol. Sci.* **374**, 20190197 (2019).
23. S. T. Frey, A. B. M. T. Haque, R. Tutika, E. V. Krotz, C. Lee, C. B. Haverkamp, E. J. Markvicka, M. D. Bartlett, Octopus-inspired adhesive skins for intelligent and rapidly switchable underwater adhesion. *Sci. Adv.* **8**, eabq1905 (2022).
24. M. Ghannoum, M. Parsek, M. Whiteley, P. Mukherjee, *Microbial Biofilms* (ASM Press, Washington, DC, ed. 2, 2015).
25. H.-C. Flemming, J. Wingender, U. Szewzyk, P. Steinberg, S. A. Rice, S. Kjelleberg, Biofilms: An emergent form of bacterial life. *Nat. Rev. Microbiol.* **14**, 563–575 (2016).
26. H.-C. Flemming, T. R. Neu, D. J. Wozniak, The EPS matrix: The "house of biofilm cells". *J. Bacteriol.* **189**, 7945–7947 (2007).
27. L. Hobley, C. Harkins, C. E. Macphee, N. R. Stanley-Wall, Giving structure to the biofilm matrix: An overview of individual strategies and emerging common themes. *FEMS Microbiol. Rev.* **39**, 649–669 (2015).

Downloaded from https://www.science.org on November 20, 2026

28. L. Hall-Stoodley, J. W. Costerton, P. Stoodley, Bacterial biofilms: From the natural environment to infectious diseases. *Nat. Rev. Microbiol.* **2**, 95–108 (2004).
29. H.-C. Flemming, S. Wuertz, Bacteria and archaea on Earth and their abundance in biofilms. *Nat. Rev. Microbiol.* **17**, 247–260 (2019).
30. F. H. Yildiz, K. L. Visick, Vibrio biofilms: So much the same yet so different. *Trends Microbiol.* **17**, 109–118 (2009).
31. J. K. Teschler, D. Zamorano-Sánchez, A. S. Utada, C. J. A. Warner, G. C. L. Wong, R. G. Linington, F. H. Yildiz, Living in the matrix: Assembly and control of *Vibrio cholerae* biofilms. *Nat. Rev. Microbiol.* **13**, 255–268 (2015).
32. J. K. Teschler, C. D. Nadell, K. Drescher, F. H. Yildiz, Mechanisms underlying *Vibrio cholerae* biofilm formation and dispersion. *Annu. Rev. Microbiol.* **76**, 503–532 (2022).
33. E. J. Nelson, J. B. Harris, J. G. Morris Jr., S. B. Calderwood, A. Camilli, Cholera transmission: The host, pathogen and bacteriophage dynamic. *Nat. Rev. Microbiol.* **7**, 693–702 (2009).
34. X. Huang, T. Nero, R. Weerasekera, K. H. Matej, A. Hinbest, Z. Jiang, R. F. Lee, L. Wu, C. Chak, J. Nijjer, I. Gibaldi, H. Yang, N. Gamble, W.-L. Ng, S. A. Malaker, K. Sumigray, R. Olson, J. Yan, *Vibrio cholerae* biofilms use modular adhesins with glycan-targeting and nonspecific surface binding domains for colonization. *Nat. Commun.* **14**, 2104 (2023).
35. J. C. N. Fong, F. H. Yildiz, The *rbmBCDEF* gene cluster modulates development of rugose colony morphology and biofilm formation in *Vibrio cholerae*. *J. Bacteriol.* **189**, 2319–2330 (2007).
36. S. De, K. Kaus, S. Sinclair, B. C. Case, R. Olson, Structural basis of mammalian glycan targeting by *Vibrio cholerae* cytolysin and biofilm proteins. *PLOS Pathog.* **14**, e1006841 (2018).
37. C. Absalon, K. Van Dellen, P. I. Watnick, A communal bacterial adhesin anchors biofilm and bystander cells to surfaces. *PLOS Pathog.* **7**, e1002210 (2011).
38. A. E. Purdy, P. I. Watnick, Spatially selective colonization of the arthropod intestine through activation of *Vibrio cholerae* biofilm formation. *Proc. Natl. Acad. Sci. U.S.A.* **108**, 19737–19742 (2011).
39. K. Barrasso, D. Chac, M. D. Debela, C. Geigel, J. B. Harris, R. C. LaRocque, F. S. Midani, F. Qadri, J. Yan, A. A. Weil, W.-L. Ng, Impact of a human gut microbe on *Vibrio cholerae* host colonization through biofilm enhancement. *eLife* **11**, e73010 (2022).
40. A. Potapova, W. Garvey, P. Dahl, S. Guo, Y. Chang, C. Schwechheimer, M. A. Trebino, K. A. Floyd, B. S. Phinney, J. Liu, N. S. Malvankar, F. H. Yildiz, Outer membrane vesicles and the outer membrane protein OmpU govern *Vibrio cholerae* biofilm matrix assembly. *MBio* **15**, e03304–23 (2024).
41. A. L. Gallego-Hernandez, W. H. DePas, J. H. Park, J. K. Teschler, R. Hartmann, H. Jeckel, K. Drescher, S. Beyhan, D. K. Newman, F. H. Yildiz, Upregulation of virulence genes promotes *Vibrio cholerae* biofilm hyperinfectivity. *Proc. Natl. Acad. Sci. U.S.A.* **117**, 11010–11017 (2020).
42. J. C. N. Fong, K. A. Syed, K. E. Klose, F. H. Yildiz, Role of *Vibrio* polysaccharide (vps) genes in VPS production, biofilm formation and *Vibrio cholerae* pathogenesis. *Microbiology* **156**, 2757–2769 (2010).
43. A. A. Bridges, M. S. Jentzsch, P. W. Oakes, P. Occhipinti, A. S. Gladfelter, Micron-scale plasma membrane curvature is recognized by the septin cytoskeleton. *J. Cell Biol.* **213**, 23–32 (2016).
44. X. Huang, R. Prasad, S. Saluja, Y. Yang, Q. Yan, S. O. Shuster, E. Karatekin, R. Olson, C. Lin, C. M. Davis, X. Jiang, H.-X. Zhou, J. Yan, Conformations and sequence determinants in the lipid binding of an adhesive peptide derived from *Vibrio cholerae* biofilms. *PLOS Pathog.* **22**, e1013990 (2026).
45. S. Erlendsson, K. Teilum, Binding revisited—avidity in cellular function and signaling. *Front. Mol. Biosci.* **7**, 615565 (2021).
46. M. Rodahl, B. Kasemo, A simple setup to simultaneously measure the resonant frequency and the absolute dissipation factor of a quartz crystal microbalance. *Rev. Sci. Instrum.* **67**, 3238–3241 (1996).
47. J. L. Jordan, E. J. Fernandez, QCM-D sensitivity to protein adsorption reversibility. *Biotechnol. Bioeng.* **101**, 837–842 (2008).
48. X. Qiao, X. Zhang, Y. Tian, Y. Meng, Progresses on the theory and application of quartz crystal microbalance. *Appl. Phys. Rev.* **3**, 031106 (2016).
49. C. B. Ching, K. Hidajat, M. S. Uddin, Evaluation of equilibrium and kinetic parameters of smaller molecular size amino acids on KX zeolite crystals via liquid chromatographic techniques. *Sep. Sci. Technol.* **24**, 581–597 (1989).
50. V. Berk, J. C. N. Fong, G. T. Dempsey, O. N. Develioglu, X. W. Zhuang, J. Liphardt, F. H. Yildiz, S. Chu, Molecular architecture and assembly principles of *Vibrio cholerae* biofilms. *Science* **337**, 236–239 (2012).
51. Z. Chen, Y. R. Shen, G. A. Somorjai, Studies of polymer surfaces by sum frequency generation vibrational spectroscopy. *Annu. Rev. Phys. Chem.* **53**, 437–465 (2002).
52. E. C. Y. Yan, L. Fu, Z. Wang, W. Liu, Biological macromolecules at interfaces probed by chiral vibrational sum frequency generation spectroscopy. *Chem. Rev.* **114**, 8471–8498 (2014).
53. Y. R. Shen, Surface properties probed by second-harmonic and sum-frequency generation. *Nature* **337**, 519–525 (1989).
54. S. Hosseinpour, S. J. Roeters, M. Bonn, W. Peukert, S. Woutersen, T. Weidner, Structure and dynamics of interfacial peptides and proteins from vibrational sum-frequency generation spectroscopy. *Chem. Rev.* **120**, 3420–3465 (2020).
55. L. Fu, Z. Wang, E. C. Y. Yan, N-H stretching modes around 3300 wavenumber from peptide backbones observed by chiral sum frequency generation vibrational spectroscopy. *Chirality* **26**, 521–524 (2014).
56. A. Barth, Infrared spectroscopy of proteins. *Biochim. Biophys. Acta* **1767**, 1073–1101 (2007).
57. M. Rabe, D. Verdes, S. Seeger, Understanding protein adsorption phenomena at solid surfaces. *Adv. Colloid Interface Sci.* **162**, 87–106 (2011).
58. D. Tabor, Surface forces and surface interactions. *J. Colloid Interface Sci.* **58**, 2–13 (1977).
59. D. Maugis, Adhesion of spheres: The JKR-DMT transition using a dugdale model. *J. Colloid Interface Sci.* **150**, 243–269 (1992).
60. S. T. Ahmed, S. Zhai, X. Huang, S. Sulaja, A. Adewole, A. Ioffe, A. D. Merg, J. Yan, R. C. Andresen Eguiluz, *Vibrio cholerae* adhesin-derived peptides mediate strong pull-off forces in aqueous media with high ionic strength. *Colloids Surf. B Biointerfaces* **260**, 115390 (2026).
61. G. Schmidt, P. E. Christ, P. E. Kertes, R. V. Fisher, L. J. Miles, J. J. Wilker, Underwater bonding with a biobased adhesive from tannic acid and zein protein. *ACS Appl. Mater. Interfaces* **15**, 32863–32874 (2023).
62. S. Jiang, Z. Cao, Ultralow-fouling, functionalizable, and hydrolyzable zwitterionic materials and their derivatives for biological applications. *Adv. Mater.* **22**, 920–932 (2010).
63. E. Johnston, M. Farrow, R. Williston, J. Wu, Z. Yang, A. Bahmani, Y. Liu, X. Huang, S. Guo, J. Yan, J. Li, Bacteria-mimetic bioadhesives with multivalent mucoadhesion and drug-compatible delivery. *Mater. Horiz.* **13**, 8580–8590 (2026).
64. Y. Yang, J. Yan, R. Olson, X. Jiang, Comprehensive genomic and evolutionary analysis of biofilm matrix clusters and proteins in the *Vibrio* genus. *mSystems* **10**, e00060–25 (2025).
65. N. Kumar, S. Dalvi, A. V. Sumant, L. Pastewka, T. D. B. Jacobs, A. Dhinojwala, Small-scale roughness entraps water and controls underwater adhesion. *Sci. Adv.* **10**, eadn8343 (2024).
66. Y. Shin, C. P. Brangwynne, Liquid phase condensation in cell physiology and disease. *Science* **357**, eaaf4382 (2017).
67. D. Bracha, M. T. Walls, C. P. Brangwynne, Probing and engineering liquid-phase organelles. *Nat. Biotechnol.* **37**, 1435–1445 (2019).
68. R. van der Lee, M. Buljan, B. Lang, R. J. Weatheritt, G. W. Daughdrill, A. K. Dunker, M. Fuxreiter, J. Gough, J. Gsponer, D. T. Jones, P. M. Kim, R. W. Kriwacki, C. J. Oldfield, R. V. Pappu, P. Tompa, V. N. Uversky, P. E. Wright, M. M. Babu, Classification of intrinsically disordered regions and proteins. *Chem. Rev.* **114**, 6589–6631 (2014).
69. H.-X. Zhou, D. Kota, S. Qin, R. Prasad, Fundamental aspects of phase-separated biomolecular condensates. *Chem. Rev.* **124**, 8550–8595 (2024).
70. K. Sugase, H. J. Dyson, P. E. Wright, Mechanism of coupled folding and binding of an intrinsically disordered protein. *Nature* **447**, 1021–1025 (2007).
71. M. C. Wilson, Q. Lu, K. R. Nachtrieb, J. S. Fuller, C. M. Skogg, E. A. Yates, M. D. Thum, C. R. So, Underwater adhesives produced by chemically induced protein aggregation. *Adv. Funct. Mater.* **34**, 2308790 (2024).
72. C. R. Frihart, C. G. Hunt, M. J. Birkeland, "Soy proteins as wood adhesives" in *Recent Advances in Adhesion Science and Technology* (2014), pp. 277–290.
73. S. Beyhan, F. H. Yildiz, Smooth to rugose phase variation in *Vibrio cholerae* can be mediated by a single nucleotide change that targets c-di-GMP signalling pathway. *Mol. Microbiol.* **63**, 995–1007 (2007).
74. A. B. Dalia, E. McDonough, A. Camilli, Multiplex genome editing by natural transformation. *Proc. Natl. Acad. Sci. U.S.A.* **111**, 8937–8942 (2014).
75. G. Sauerbrey, Verwendung von Schwingquarzen zur Wagung dunner Schichten und zur Mikrowagung. *Z. Physik* **155**, 206–222 (1959).
76. S. Jo, T. Kim, V. G. Iyer, W. Im, CHARMM-GUI: A web-based graphical user interface for CHARMM. *J. Comput. Chem.* **29**, 1859–1865 (2008).
77. H. J. Feldman, C. W. V. Hogue, Probabilistic sampling of protein conformations: New hope for brute force? *Proteins* **46**, 8–23 (2002).
78. F. S. Emami, V. Puddu, R. J. Berry, V. Varshney, S. V. Patwardhan, C. C. Perry, H. Heinz, Force field and a surface model database for silica to simulate interfacial properties in atomic resolution. *Chem. Mater.* **26**, 2647–2658 (2014).
79. J. Huang, S. Rauscher, G. Nawrocki, T. Ran, M. Feig, B. L. De Groot, H. Grubmüller, A. D. MacKerell Jr., CHARMM36m: An improved force field for folded and intrinsically disordered proteins. *Nat. Methods* **14**, 71–73 (2017).
80. W. L. Jorgensen, J. Chandrasekhar, J. D. Madura, R. W. Impey, M. L. Klein, Comparison of simple potential functions for simulating liquid water. *J. Chem. Phys.* **79**, 926–935 (1983).
81. J. C. Phillips, R. Braun, W. Wang, J. Gumbart, E. Tajkhorshid, E. Villa, C. Chipot, R. D. Skeel, L. Kalé, K. Schulten, Scalable molecular dynamics with NAMD. *J. Comput. Chem.* **26**, 1781–1802 (2005).
82. U. Essmann, L. Perera, M. L. Berkowitz, T. Darden, H. Lee, L. G. Pedersen, A smooth particle mesh Ewald method. *J. Chem. Phys.* **103**, 8577–8593 (1995).

Downloaded from https://www.science.org on November 20, 2026

83. J.-P. Ryckaert, G. Ciccotti, H. J. C. Berendsen, Numerical integration of the cartesian equations of motion of a system with constraints: Molecular dynamics of *n*-alkanes. *J. Comput. Phys.* **23**, 327–341 (1977).
84. S. E. Feller, Y. Zhang, R. W. Pastor, B. R. Brooks, Constant pressure molecular dynamics simulation: The Langevin piston method. *J. Chem. Phys.* **103**, 4613–4621 (1995).
85. D. R. Roe, T. E. Cheatham III, PTRAJ and CPPTRAJ: Software for processing and analysis of molecular dynamics trajectory data. *J. Chem. Theory Comput.* **9**, 3084–3095 (2013).
86. W. Humphrey, A. Dalke, K. Schulten, VMD: Visual molecular dynamics. *J. Mol. Graph.* **14**, 33–38 (1996).
87. E. A. Perets, D. Konstantinovsky, T. Santiago, P. E. Videla, M. Tremblay, L. Velarde, V. S. Batista, S. Hammes-Schiffer, E. C. Y. Yan, Beyond the "spine of hydration": Chiral SFG spectroscopy detects DNA first hydration shell and base pair structures. *J. Chem. Phys.* **161**, 095104 (2024).
88. G. Ma, J. Liu, L. Fu, E. C. Y. Yan, Probing water and biomolecules at the air-water interface with a broad bandwidth vibrational sum frequency generation spectrometer from 3800 to 900 cm^{-1}. *Appl. Spectrosc.* **63**, 528–537 (2009).
89. A. Beaussart, S. El-Kirat-Chatel, R. M. A. Sullan, D. Alsteens, P. Herman, S. Derclaye, Y. F. Dufrêne, Quantifying the forces guiding microbial cell adhesion using single-cell force spectroscopy. *Nat. Protoc.* **9**, 1049–1055 (2014).
90. K. Kaus, A. Biester, E. Chupp, J. Lu, C. Visudharomn, R. Olson, The 1.9 Å crystal structure of the extracellular matrix protein Bap1 from *Vibrio cholerae* provides insights into bacterial biofilm adhesion. *J. Biol. Chem.* **294**, 14499–14511 (2019).

Acknowledgments

Funding: This research was developed with funding from the Defense Advanced Research Projects Agency (DARPA HR00112430356 to J.Y. and HR00112430362 to R.A.E.). The views, opinions, and/or findings expressed are those of the authors and should not be interpreted as representing the official views or policies of the Department of Defense or the US Government. J.Y. also acknowledges the support from Burroughs Wellcome Fund (#1022835). R.P. and H.-X.Z. were supported by NIH grant R35 GM118091. P.D. and N.M. were supported by the US Department of Energy (DE-SC0025520) and the US National Science Foundation–Molecular and Cellular Biosciences (no. 2522073) and Physics of Living Systems (no. 2609934). Z.W. and E.C.Y.Y. were supported by the NIH (R35GM156522). R.A.J. was supported by the NIH (T32GM149438). The content is solely the responsibility of the authors and does not necessarily represent the official views of the National Institutes of Health. Additional support was provided to R.O. by Wesleyan University Grants in Support of Scholarship funds. M.E.M. acknowledges the NIST Cooperative Agreement Nos. 70NANB20H139 and 70NANB23H226 for support. Certain commercial materials, equipment, and instruments are identified in this work to describe the experimental procedure as completely as possible. In no case does such an identification imply a recommendation or endorsement by NIST, nor does it imply that the materials, equipment, or instruments identified are necessarily the best available for the purpose. Unless otherwise noted, NIST work was funded solely by the United States Government. **Author contributions:** X.H. and J.Y. conceptualized the project. X.H. performed strain construction and validation. X.H. performed bead-based assays and quantification. X.H. performed adsorption assays and biofilm imaging. M.E.M. performed QCM-D measurement and data analysis. X.H. and P.D. performed the AFM measurement. R.P. and H.-X.Z. performed MD simulations and analyzed MD data. Y.L. performed lap shear measurements. E.D.L. and M.W. obtained the peptide from *E. coli*. E.L. and S.S. performed the flocculation assay. Z.W., R.A.J., and E.C.Y.Y. performed the SFG measurements and data analysis. X.H., R.P., Z.W., M.E.M., E.C.Y.Y., H.-X.Z., and J.Y. wrote the manuscript. All authors contributed to the final manuscript. **Competing interests:** J.Y. and R.O. are inventors on patent application (US19/112,977) submitted by Yale University and Wesleyan University that covers the use of the Bap1-derived as adhesives. The patent was filed on 20 September 2023 and published on 16 April 2026 (publication number: US20260103629). All other authors declare that they have no competing interests. **Data, code, and materials availability:** All data and code needed to evaluate the conclusions in the paper are present in the paper and/or the Supplementary Materials. New peptides synthesized in the project can be ordered through the specified vendors. All bacterial strains and peptides constructed as part of this work will be provided to the community upon request in a timely fashion and shipped in accordance with biosafety standards and regulations; all requests should be addressed to J.Y. (jing.yan@yale.edu).

Submitted 19 April 2026
Accepted 30 September 2026
Published 4 November 2026
10.1126/sciadv.aei1795

Downloaded from https://www.science.org on November 20, 2026

ScienceAdvances

A biofilm-derived peptide as an underwater adhesive

Xin Huang, Ewelina D. Liszczyk, Ramesh Prasad, Megan E. Mitchell, Zhijie Wang, Yuchu Liu, Sarvagya Saluja, Mingyu Wang, Rebekah A. Jackson, Peter Dahl, Roberto Andresen Eguiluz, Nikhil Malvankar, Elsa C. Y. Yan, Rich Olson, Huan-Xiang Zhou, and Jing Yan

Sci. Adv. **12** (45), eaei1795. DOI: 10.1126/sciadv.aei1795

View the article online
https://www.science.org/doi/10.1126/sciadv.aei1795
Permissions
https://www.science.org/help/reprints-and-permissions

Downloaded from https://www.science.org on November 20, 2026

Use of this article is subject to the Terms of service

Science Advances (ISSN 2375-2548) is published by the American Association for the Advancement of Science. 1200 New York Avenue NW, Washington, DC 20005. The title *Science Advances* is a registered trademark of AAAS.

Copyright © 2026 The Authors, some rights reserved; exclusive licensee American Association for the Advancement of Science. No claim to original U.S. Government Works. Distributed under a Creative Commons Attribution NonCommercial License 4.0 (CC BY-NC).